Ⓔ

Stochastic Strong Ground Motion Simulation of the Southern Aegean Sea Benioff Zone Intermediate-Depth Earthquakes

by Ch. Kkallas, C. B. Papazachos, B. N. Margaris, D. Boore, Ch. Ventouzi, and A. Skarlatoudis

Abstract   We employ the stochastic finite-fault modeling approach of Motazedian and Atkinson (2005), as adapted by Boore (2009), for the simulation of Fourier amplitude spectra (FAS) of intermediate-depth earthquakes in the southern Aegean Sea subduction (southern Greece). To calibrate the necessary model parameters of the stochastic finite-fault method, we used waveform data from both acceleration and broadband-velocity sensor instruments for intermediate-depth earthquakes (depths ∼45–140 km) with **M** 4.5–6.7 that occurred along the southern Aegean Sea Wadati–Benioff zone. The anelastic attenuation parameters employed for the simulations were adapted from recent studies, suggesting large back-arc to fore-arc attenuation differences. High-frequency spectral slopes (kappa values) were constrained from the analysis of a large number of earthquakes from the high-density EGELADOS (Exploring the Geodynamics of Subducted Lithosphere Using an Amphibian Deployment of Seismographs) temporary network. Because of the lack of site-specific information, generic site amplification functions available for the Aegean Sea region were adopted. Using the previous source, path, and site-effect constraints, we solved for the stress-parameter values by a trial-and-error approach, in an attempt to fit the FAS of the available intermediate-depth earthquake waveforms. Despite the fact that most source, path, and site model parameters are based on independent studies and a single source parameter (stress parameter) is optimized, an excellent comparison between observations and simulations is found for both peak ground acceleration (PGA) and peak ground velocity (PGV), as well as for FAS values. The final stress-parameter values increase with moment magnitude, reaching large values (> 300 bars) for events **M** ≥ 6.0. Blind tests for an event not used for the model calibration verify the good agreement of the simulated and observed ground motions for both back-arc and along-arc stations. The results suggest that the employed approach can be efficiently used for the modeling of large historical intermediate-depth earthquakes, as well as for seismic hazard assessment for similar intermediate-depth events in the southern Aegean Sea area.

Electronic Supplement: Input parameter file for program EXSIM_DMB and tables of site amplification factors.

Introduction

Greece is located along the most active tectonic plate boundary in Europe, where the eastern Mediterranean oceanic-type lithosphere subducts beneath the Aegean Sea microplate (Fig. 1). As a result, strong intermediate-depth earthquakes occur along the South Aegean Sea arc, either as interface earthquakes along the outer-arc (depths typically in the 45–60 km range) or as in-slab earthquakes forming the deeper part of the South Aegean Sea Wadati–Benioff zone (depths ≥ 60 km). Although in-slab and interface events are different, their strong-motion properties have often been jointly examined worldwide (e.g., Atkinson and Boore, 2003; Zhao *et al.*, 2006; Abrahamson *et al.*, 2015), as well as for the Aegean Sea area (Skarlatoudis *et al.*, 2013), because the subduction area attenuation and the effect of source depth are similar for both event types. The stronger events (e.g., the A.D. 365 **M** 8.2 interface earthquake in west Crete, Shaw *et al.*, 2008; Stiros, 2010, or the 1926 **M** ∼ 8.0 Rhodes in-slab earthquake, Ambraseys and Adams, 1998) occur in
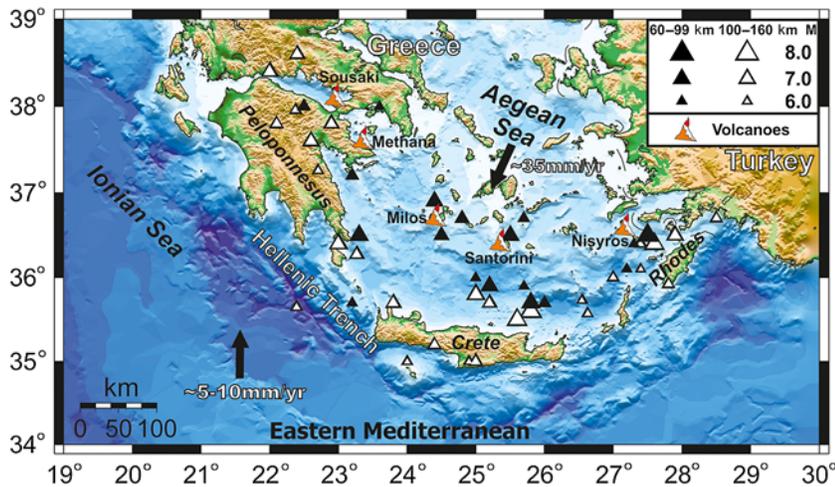
Figure 1. Schematic geotectonic map of the southern Aegean Sea subduction. Plate motions relative to stable Europe are depicted by solid vectors. The main volcanic centers of the southern Aegean volcanic arc, as well as major Benioff-zone intermediate depth events with $M \geq 6.0$ after 1800 are also shown. The color version of this figure is available only in the electronic edition.

the shallower segment of the Benioff zone ($h \leq 100$ km), whereas events up to $M \sim 7.0$ take place in its deeper part ($h \sim 100$–170 km; e.g., the $M \sim 7.0$ aftershock of the 1956 M 7.5 Amorgos shallow mainshock, Brüstle *et al.*, 2014).

Several tomographic studies (e.g., Spakman *et al.*, 1993; Papazachos *et al.*, 1995; Ventouzi *et al.*, 2014) revealed the presence of a low body-wave velocity and quality factor (high attenuation) region at the depth of $\sim$60–90 km beneath the volcanic arc (see Fig. 2). This pattern is usually attributed to the subduction process, which results in the presence of

Figure 2. Schematic seismic wave propagation for the southern Aegean Sea intermediate-depth events, along an arc-normal profile (parallel to subduction direction). Black dashed and dotted lines correspond to rays from in-slab events that cross or avoid the low Q_S–V_S back-arc mantle wedge, respectively. Black solid lines depict rays traveling through the high Q_S–V_S subducting slab. Gray solid and dashed lines delineate rays from interface events that propagate through the eastern Mediterranean and Aegean Sea crust and uppermost mantle, respectively. Vertical projections of typical fault-plane solutions are also shown (modified from Skarlatoudis *et al.*, 2013). The color version of this figure is available only in the electronic edition.

partial melt and/or significant volatile content in the high-temperature mantle wedge above the subducting eastern Mediterranean plate. As a result, mainly S (but also P) waves from intermediate-depth earthquakes are strongly attenuated along the South Aegean Sea volcanic arc. Because of this attenuation pattern, large differences between the corresponding fore-arc and back-arc seismic motions have been observed, roughly reaching up to 1 order of magnitude (e.g., Papazachos and Comninakis, 1969, 1971; Boore *et al.*, 2009; Skarlatoudis *et al.*, 2013) for sites at similar distances from the source.

Figure 2 presents a conceptual model of the geotectonic setting and the seismic wave propagation pattern for intermediate-depth earthquakes in the southern Aegean Sea subduction area (modified from Skarlatoudis *et al.*, 2013; hereafter, Sea13). The propagation of direct P and S waves for in-slab events through the low-V_S/low-Q_S mantle wedge under the volcanic arc results in their strong attenuation. In contrast, waves from in-slab events propagating toward the outer Hellenic arc exhibit relative high-frequency amplification, as smaller wavelengths are channeled through the subducted (high-V_S/high-Q_S) eastern Mediterranean lithosphere. This model suggests that the fore-arc to back-arc differences are expected to be more prominent for deeper events, a pattern recognized also in the macroseismic effects of large historical intermediate-depth events (Papazachos and Comninakis, 1969, 1971; Papadopoulos *et al.*, 2002). On the other hand, seismic waves from interface events mostly propagate through the eastern Mediterranean and Aegean Sea lithospheres (see Fig. 2) and are not affected by the volcanic-arc mantle wedge, hence the corresponding seismic-motion parameters (peak ground acceleration [PGA], peak ground velocity [PGV], etc.) mostly reflect the average lithospheric attenuation properties.

The stochastic simulation of strong ground motions is widely recognized as one of the most important tools for the modeling of observed and expected ground motions from strong earthquakes. Although the application of stochastic simulation for shallow earthquakes has been adopted by several researchers in Greece (e.g., Margaris and Boore, 1998; Roumelioti *et al.*, 2000, 2004; Margaris and Hatzidimitriou, 2002; Boore *et al.*, 2009) and worldwide (e.g., Castro *et al.*, 2001; Arrigo *et al.*, 2006; Motazedian, 2006; Boore *et al.*, 2010; Ugurhan and Askan, 2010; Ameri
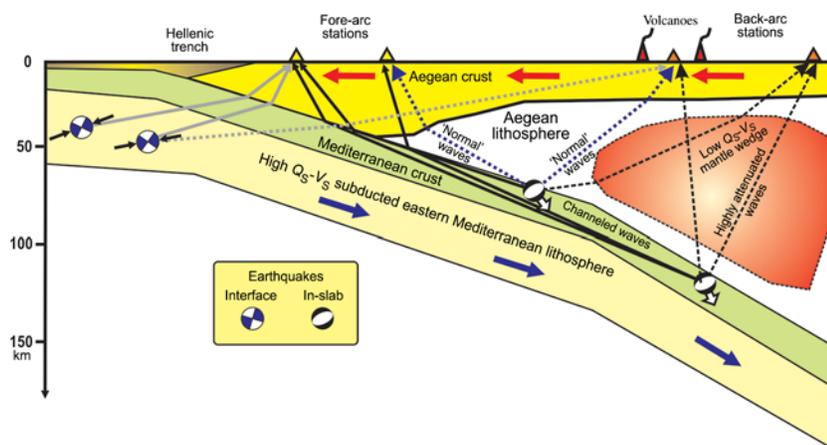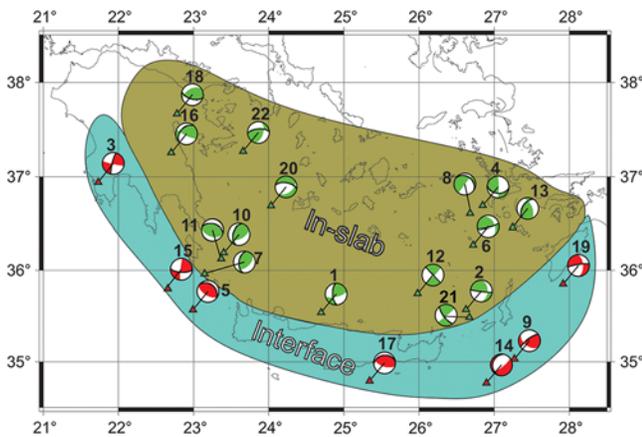
Figure 3. Focal mechanisms of the in-slab and interface intermediate-depth earthquakes for the southern Aegean Sea subduction area used in the present study (numbers correspond to the ID column of Table 1). The color version of this figure is available only in the electronic edition.

et al., 2011; Yazdani and Kowsari, 2013), its applications for the study of intermediate-depth earthquakes are very limited. Benetatos and Kiratzi (2004) applied the method of Beresnev and Atkinson (1997) for the intermediate-depth earthquake of Karpathos (22 January 2002, **M** 6.1, $h = 91$ km), showing good correlation of the observed and simulated acceleration Fourier amplitude spectra (FAS) for fore-arc stations (back-arc high attenuation was not considered in their study).

In the present work, we present a systematic approach to model southern Aegean intermediate-depth events ($h > 45$ km) using the stochastic simulation technique. To perform this modeling, we base our analysis on the conceptual model of Figure 2, as well as on published results (e.g., Boore *et al.*, 2009; Yolsal-Çevikbilen and Taymaz, 2012) for the study area regarding the source, path, and site-effect properties. More specifically, we introduce different attenuation functions for the back-arc and fore-arc subduction area on the basis of previous work (Skarlatoudis *et al.*, 2013). We model directly the acceleration FAS, optimizing only the stress parameter, in an attempt to generate a model that can efficiently reproduce both spectral and time-series measures for the events studied. We preferred to employ a finite-fault simulation approach, with a simple source modeling scheme, to be able to apply the model also to larger intermediate-depth events. The whole approach is formulated on the basis of a small number of well-constrained parameters (event magnitude and typical or determined fault-plane solution), to allow its easier application for reliable ground-motion prediction for future intermediate-depth events in the study area. Moreover, the proposed approach can be easily adapted for the study of historical, damaging intermediate-depth events that have occurred in the southern Aegean Sea subduction zone, for which only macroseismic information is available. Finally, we perform a model verification with a blind test on an earthquake not used for the model calibration.

Modeling ground motions for the southern Aegean Sea intermediate-depth earthquakes with the stochastic simulation approach requires consideration of (a) the poor knowledge of intermediate-depth seismic source parameters (i.e., although focal mechanisms follow a certain spatial pattern, the actual fault is unknown or poorly understood due to the lack of, e.g., directivity analysis studies), as well as the fact that such events have practically nonexisting aftershock sequences; (b) the observed waveforms exhibit complicated patterns, for example, very small amplitude S phases in the back-arc area (due to anelastic attenuation) or hidden in the P-wave coda in the fore-arc area (due to multipathing/multiple scattering); and (c) the lack of high-quality data, as recording networks are rather sparse and very few strong intermediate-depth events have been recorded. On the other hand, several features of the intermediate-depth earthquakes in the study area (e.g., 3D attenuation model, attenuation of PGA or PGV, etc.) have been relatively recently investigated in more detail (e.g., Skarlatoudis and Margaris, 2006; Boore *et al.*, 2009; Skarlatoudis *et al.*, 2013; Ventouzi *et al.*, 2013, 2014), and were used as a basis for the application of the stochastic simulation for intermediate-depth events.

Data Used

Despite the relatively small number of intermediate-depth earthquakes for which seismic records are available, a large number of good quality waveform data covering the southern Aegean Sea subduction zone have been used to calibrate the main stochastic modeling parameters on the basis of peak ground-motion measures (PGA and PGV) and FAS values. Figure 3 presents the focal mechanisms of the examined events, collected from published information or constrained using the dominant style-of-faulting and orientation from Kkallas *et al.* (2013). Table 1 presents the seismological information for each earthquake. Moment magnitudes were collected from the same studies, though for event 14 we used its equivalent moment magnitude (**M**∗) from Sea13. The final database includes 22 earthquakes which occurred between 1994 and 2014, containing 610 horizontal-component recordings (Table 1).

The intermediate-depth event dataset was divided into two subsets, namely interface events located along the outer Hellenic arc with depths from 45 to 60 km (**M** 4.6–6.4), and in-slab events located in the inner arc with depths from 60 to 140 km (**M** 4.5–6.7), also listed in Table 1 (column CR, 7 interface and 15 in-slab events). For each earthquake, the fault employed for the stochastic simulation approach (thick black lines on the focal mechanisms of Fig. 3) has been adopted from Kkallas *et al.* (2013). This fault-plane selection was based on directivity analysis (mainly for large events such as the Kythera event, Benetatos and Kiratzi, 2006), compatibility with fault observations (e.g., north-dipping plane for interface events in the outer-arc), stress inversion and previously proposed fault directions in various studies (e.g., Papazachos, 1990). In any case, tests with alternative

Table 1
Information on the Earthquakes for Data Used in the Present Study

ID	Origin Time (yyyy/mm/dd hh:mm:ss)	Latitude (°)	Longitude (°)	Depth (km)	M	CR[†]	Az (°)	Dip (°)	Rake (°)	Source	Records Used	Stress Parameters (bars)
1	1994/05/23 06:46:12	35.5409	24.6968	68	6.1	0	177	63	22	ISC-Global CMT	6	400
2	2002/01/22 04:53:52	35.5740	26.6270	90	6.1	0	97	86	49	Benetatos and Kiratzi (2004)	16	300
3	2003/04/29 01:51:20	36.9395	21.7314	66	5.1	1	193	81	4	ISC-Global CMT	10	300
4	2003/09/13 13:46:21	36.6910	26.8488	134	5.2	0	97	40	10	CYG-Global CMT	24	70
5	2004/03/28 14:54:38	35.5700	22.9900	55	4.7	1	310	31	97	Global CMT	30	20
6	2004/10/07 01:05:12	36.2700	26.7200	130	5.5	0	75	81	50	Global CMT	30	130
7	2004/11/04 06:22:37	35.9633	23.1454	70	5.2	0	187	48	58	ISC-Global CMT	30	400
8	2005/08/01 13:34:58	36.6092	26.6775	127	4.8	0	306	27	180	EGE-Global CMT	26	100
9	2005/11/20 21:20:56	35.0332	27.2676	50	4.6	1	233	75	44	ISC-NOA	32	30
10	2006/01/08 11:34:54	36.1853	23.4037	67	6.7	0	197	45	53	Benetatos and Kiratzi (2006)	34	400
11	2006/05/11 01:47:47	36.1256	23.3697	72	4.5	0	285	43	87	ISC-NOA	40	50
12	2006/05/15 04:22:39	35.7490	25.9830	68	4.7	0	316	88	−10	EGE-NOA	28	50
13	2006/07/09 03:12:54	36.4597	27.2451	118	4.6	0	212	50	133	ISC-NOA	34	100
14	2006/12/02 10:26:54	34.7687	26.8962	52	4.7*	1	196	20	−124	ISC-NOA	22	300
15	2007/02/03 13:43:22	35.8092	22.6367	47	5.4	1	93	68	173	EGE-Global CMT	30	45
16	2008/01/06 05:14:20	37.2569	22.7037	84	6.2	0	222	41	20	ISC-Global CMT	50	400
17	2008/03/28 00:16:19	34.7922	25.3423	49	5.6	1	264	32	69	ISC-Global CMT	16	100
18	2008/06/18 01:58:42	37.6700	22.7800	83	5.1	0	107	58	122	ISC-Global CMT	36	350
19	2008/07/15 03:26:34	35.8500	27.9200	56	6.4	1	261	81	−36	ISC-Global CMT	24	500
20	2008/09/16 02:58:39	36.6900	24.0300	137	4.5	0	280	58	−62	ISC-Global CMT	24	20
21	2011/04/01 13:29:12	35.4900	26.6700	75	6.1	0	142	71	5	ISC-Global CMT	48	400
22	2014/04/04 20:08:07	37.2700	23.6600	96	5.5	0	265	63	138	GFZ	20	100

M, moment magnitude; EGE, EGELADOS (Exploring the Geodynamics of Subducted Lithosphere Using an Amphibian Deployment of Seismographs) temporary seismological network; ISC, International Seismological Centre; Global CMT, Global Centroid Moment Tensor database; NOA, National Observatory of Athens; GFZ, GeoForschungsZentrum Potsdam.

*Equivalent moment magnitude (**M∗**) from Skarlatoudis *et al.* (2013; hereafter, Sea13) for event 14.

[†]CR, 0 for in-slab events and 1 for interface events.

fault planes suggest that this selection is not critical, especially for the larger depth and smaller-magnitude events, due to the large hypocentral distances in comparison to fault dimensions.

Recently, Skarlatoudis *et al.* (2013) proposed new ground-motion prediction equations (GMPEs) for the intermediate-depth earthquakes of the southern Aegean Sea area; these GMPEs account for the much higher peak ground motions (especially accelerations) recorded at fore-arc stations than those observed at back-arc stations. The observed large differences (up to almost 1 order of magnitude for PGA) can be easily recognized in the waveform recordings (e.g., stations NPS and APE, Fig. 4), as well as in their spectral content. The dashed line in Figure 4 depicts the limit of the back-arc high-attenuation volcanic area, as proposed and verified by Sea13. This limit was drawn on the basis of tomographic results that delineate the region of very low upper-mantle velocities ($V_P < 7.8$ km/s) for the 60–90 km depth range (Papazachos *et al.*, 1995).

The recent improvement of permanent seismological networks and the operation of temporary networks in the South Aegean Sea region have contributed to the generation of a high-quality acceleration and velocity waveform dataset

for the area. Most of the data came from the EGELADOS (Exploring the Geodynamics of Subducted Lithosphere Using an Amphibian Deployment of Seismographs) network (Friederich and Meier, 2008), which was a large temporary seismic network (65 land stations), covering almost the entire Hellenic subduction area. One of the main earthquakes considered is the 2006 Kythera intermediate-depth earthquake (**M** 6.7, depth 66 km), which occurred during the EGELADOS recording period, producing a significant number of high-quality records, partly employed in previous studies (e.g., Boore *et al.*, 2009; Skarlatoudis *et al.*, 2009, 2013). We also used broadband velocity data from the National Observatory of Athens, Aristotle University of Thessaloniki, and the GEOFON (GeoForschungsZentrum, GFZ Potsdam) permanent networks, the CYCNET (CYClades NETwork) temporary network (Bohnhoff *et al.*, 2004), which preceded the EGELADOS network, and other stations belonging to the Hellenic Unified Seismological Network. Accelerometer data from the Institute of Engineering Seismology and Earthquake Engineering and the Geodynamic Institute of the National Observatory of Athens network were also used. Finally, the original recordings from the Karpathos earthquake (**M** 6.1, $h = 90$ km) used by Benetatos and Kiratzi (2004) were also
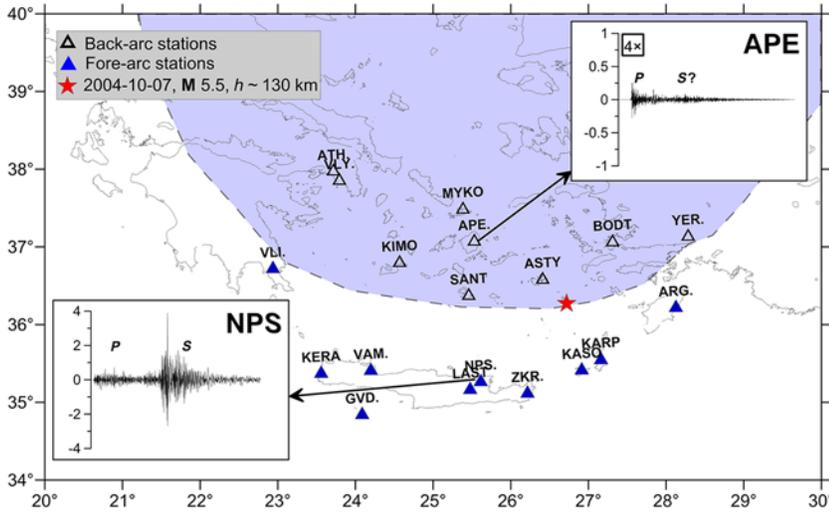
Figure 4. Recording stations for a typical intermediate-depth earthquake (7 October 2004, **M** 5.5, $h \sim 130$ km, solid star). Fore-arc and back-arc stations are shown by solid and open triangles, respectively. The shaded area depicts the high-attenuation back-arc area proposed in Skarlatoudis *et al.* (2013; hereafter, Sea13; see the Data Used section for explanation). Acceleration waveforms of the 7 October 2004 event are shown in the inset figures for two stations (APE and NPS), located roughly at the same hypocentral distance. Fore-arc station NPS exhibits typical *P*- and *S*-wave amplitudes, whereas back-arc station APE (amplitude scale multiplied by 4) shows a characteristic impulsive arrival *P* waveform, followed by very low *S* amplitudes, due to the high attenuation of *S*-wave energy within the mantle wedge beneath the volcanic arc. The color version of this figure is available only in the electronic edition.

included in our dataset. All records were corrected for instrument response and filtered to remove noise. More specifically, all broadband records were high-pass filtered by an appropriate second-order Butterworth filter after baseline correction, whereas accelerometer records were processed following
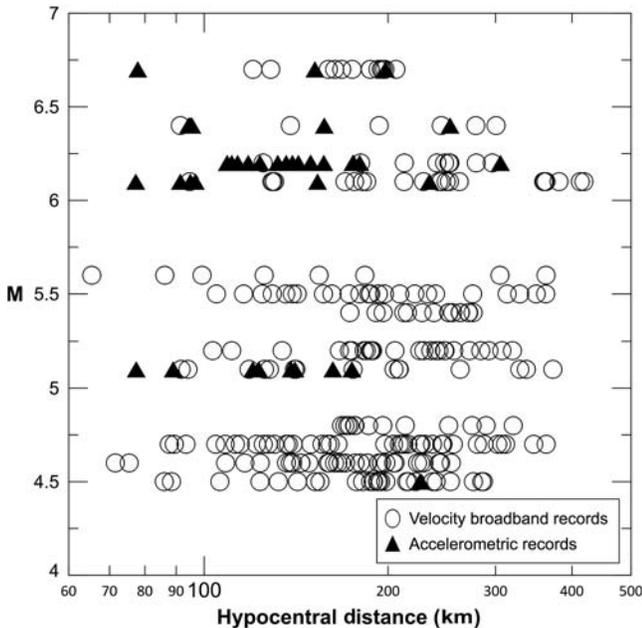

Figure 5. Magnitude–distance distribution of records employed in the present work.

Boore (2003, 2005) and Skarlatoudis and Margaris (2006). The magnitude–distance distribution of the broadband and accelerometer records (Fig. 5) reveals that although the employed dataset does not have a large number of events above **M** 6.0, the magnitude–distance space is well sampled by the available data from both types of recording instruments.

Estimation of the Stochastic Modeling Parameters

For the stochastic simulations, we used the EXSIM_DMB code by Boore (2009) who modified the original approach of Motazedian and Atkinson (2005). The stochastic method is not discussed here in detail, but the interested reader is referred to the relevant literature (e.g., Boore, 1983, 2009; Boore and Atkinson, 1987; Atkinson and Boore, 1997). The stochastic point-source model for the horizontal ground motions from each subsource in the frequency domain has the following form:

$$A_{ij}(f) = CM_{0ij}H_{ij}\left(\frac{(2\pi f)^2}{1+\left(\frac{f}{f_{0ij}(t)}\right)2}\right)(e)^{\frac{-\pi f R_{ij}}{Q(f)\beta}}G(R_{ij})D(f)e^{-\pi f \kappa_0},$$

(1)

in which $C = R_p 2^{1/2}/(4\pi\rho\beta^3)$ controls the radiation term, R_p is the radiation pattern coefficient, ρ is the density, and β is the shear-wave velocity. M_{0ij}, f_{0ij}, and R_{ij} are the ijth subfault seismic moment, corner frequency, and distance from the observation point, respectively. The scaling factor H_{ij} is used to consistently maintain high spectral frequencies for each subfault (Motazedian and Atkinson, 2005, as modified by Boore, 2009). The term $e^{-\pi f \kappa_0}$ is a high-cut filter, with the κ_0 factor representing the spectral decay at high frequencies reduced to zero distance. The corner frequency is estimated using the following equation:

$$f_{0ij}(t) = 4.9 \times 10^6 N_R(t)^{-1/3}N^{-1/3}\beta(\Delta\sigma/M_0)^{1/3}, \quad (2)$$

in which $N_R(t)$ is the cumulative number of subfaults at faulting duration time t, whereas $\Delta\sigma$ is the stress parameter in bars, M_0 is the seismic moment in dyn·cm, and β is the shear-wave velocity near the source, in km/s. $Q(f)$ is the quality factor, $G(R_{ij})$ is the geometrical spreading factor, and $D(f)$ is the site amplification. Several parameters in equations (1) and (2) (i.e., κ_0-values, Q_S model, stress parameter $\Delta\sigma$, fault geometry, and subfault distribution), as well as additional factors (e.g., site effects on ground motions) need to be defined for the stochastic simulations, as they control the physical aspects of ground motion. The parameters used in the present study
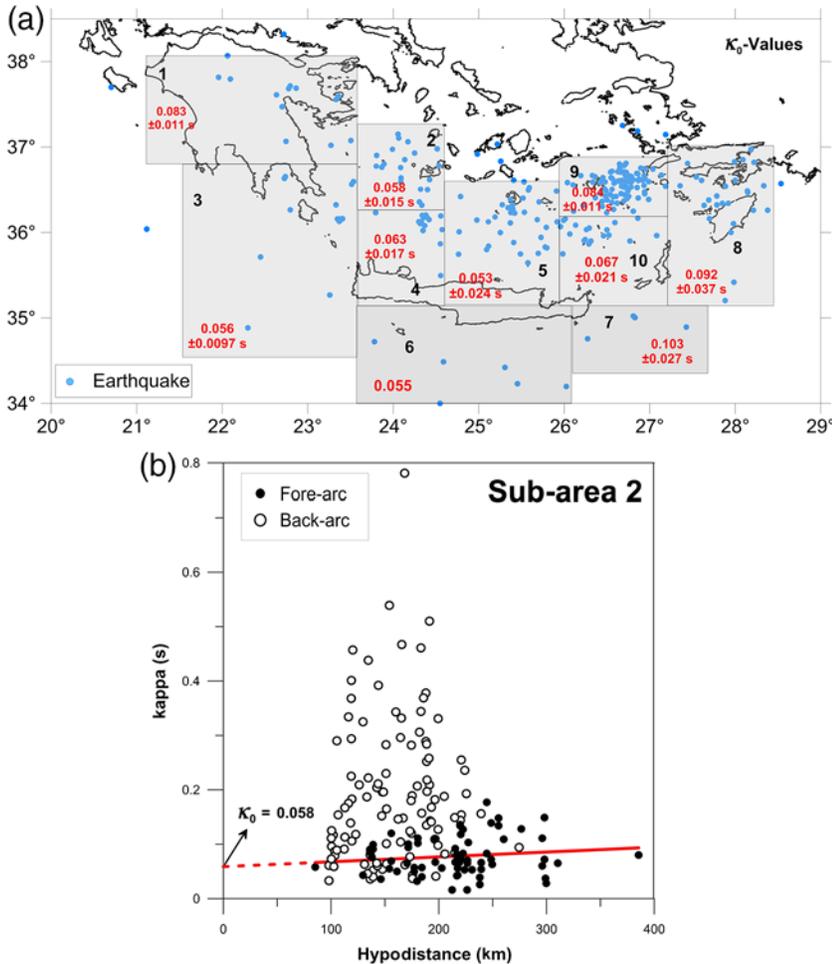
Figure 6. (a) Spatial variation of the average κ_0-values for 10 subregions of the study area, using the kappa (κ) dataset of Ventouzi *et al.* (2013) for intermediate-depth earthquakes (depicted by circles). (b) Distribution of kappa values for fore-arc (solid circles) and back-arc (open circles) stations against hypocentral distance for subarea 2. The (best-fit) line is determined using only kappa values from fore-arc stations, not affected by the high attenuation of the volcanic-arc mantle wedge. The color version of this figure is available only in the electronic edition.

were estimated from published information or have been constrained from the available data, as described in the following.

Kappa Values

We used the kappa values (κ) dataset reported by Ventouzi *et al.* (2013), as estimated from acceleration high-frequency spectral slopes from relatively small-magnitude events recorded by the CYCNET, EGELADOS, and permanent regional networks ($\sim 35,000$ values). Because the measured kappa values include anelastic attenuation effects, we obtained a zero-distance kappa estimate κ_0, assuming a simple linear hypocentral distance scaling

$$\kappa = \kappa_r R + \kappa_0 \qquad (3)$$

(e.g., Anderson and Hough, 1984). For the κ_0 determination, we excluded values reported for back-arc (volcanic-arc) stations, as these values are clearly affected by the strong attenu-

ation of the mantle wedge, later discussed in detail, because this would lead to a systematic overestimation of the κ_0-values. The average κ_0-value obtained from equation (3) for all earthquakes was ~ 0.07 s, much larger than the typical κ_0-values of 0.015–0.040 s for bedrock formations in Greece (e.g., Margaris and Boore, 1998; Ktenidou *et al.*, 2012), because almost all recording stations were located on bedrock formations (see also Skarlatoudis *et al.*, 2013). This observation suggests that an average ~ 0.03 s (or even larger) κ_0 increase is present in the employed dataset.

Although the significance of κ_0 has been an issue of extensive discussion, it is widely accepted that κ_0 mostly reflects site attenuation properties (e.g., Ktenidou *et al.*, 2014). The previously mentioned κ_0 results for bedrock fore-arc stations suggest that an additional, non-site-dependent component is present in the results. This bias could be due to (a) an additional systematic source contribution for the specific type of intermediate-depth events or (b) the presence of further attenuation in the near-source area (e.g., as suggested by Kilb *et al.*, 2012) or along the ray path that has not been appropriately corrected by the simplistic linear extrapolation of equation (3). In both cases, this contribution to κ_0 can be expected to spatially vary, due to the complicated 3D pattern of back-arc low-Q anomalies, as well as due to the depth and along-arc variations of seismic source contributions to κ_0. To study the possible spatial variability of κ_0-values, we separated the examined area into 10 subregions with common seismotectonic characteristics (Fig. 6a). The separation was based on the spatial distribution of the events for which κ data were obtained (depicted in Fig. 6a), the gradual increase of event depths toward the back-arc area, as well as the type of the corresponding typical intermediate-depth focal mechanisms (Kkallas *et al.*, 2013). As presented in Figure 6a, zones 1, 3, 6, 7, and 8 mostly cover the outer-arc, with event depths up to 100 km, whereas the remaining inner zones mainly include events with larger depths (≥ 100 km, see also Fig. 1).

As earlier noted, the κ-values for back-arc stations are heavily influenced by the very strong effect of the low-velocity/low-Q mantle wedge on the high-frequency waveform content. Therefore, for each subregion of Figure 6a we have used only κ-values from fore-arc stations (to avoid the contribution of the back-arc high attenuation) to determine an average κ_0-value. A typical example is presented in Figure 6b, where the κ-values from Ventouzi *et al.* (2013) for zone 2 in

Figure 6a are presented against hypocentral distance. It is clear that the back-arc data do not follow the roughly linear trend (distance increase) of fore-arc data, as their values are controlled by the high volcanic-arc attenuation, and should be neglected from any κ_0 analysis.

The average κ_0-values for fore-arc stations, as presented in Figure 6a, vary in the ~0.05–0.10 range, with a median value of ~0.065. It should be noticed that a good agreement of the κ_0-value defined for subarea 3 (0.056) is observed with the κ_0 estimate of 0.055 obtained by Boore et al. (2009) only for the 2006 Kythera earthquake that occurred in the same subarea. Moreover, similar large κ_0-values (~0.07) have been observed for several hard-rock stations by Sokolov et al. (2005) for Vrancea intermediate-depth events. More recently, Pavel and Vacareanu (2015) confirmed the very large κ_0-values at bedrock stations in the Vrancea epicentral area (~0.10) for intermediate-depth events, reducing to lower (but still high) κ_0-values (~0.06–0.07) for the outer-arc (lower attenuation) region, similar to the results presented here. These observations, as well as the systematically high κ_0-values presented in Figure 6a for all subregions, suggest that such high κ_0 bedrock values should be considered as a robust feature of the southern Aegean Sea subduction zone events, that needs to be appropriately considered for the stochastic modeling. It is important to note that the proposed κ_0-values show a significant spatial variability along the southern Aegean subduction zone, with spatial variations being significantly larger than the associated κ_0 errors, also presented in Figure 6a. For this reason, different κ_0-values were adopted for each earthquake simulation, depending on the location of the event for which ground motions are being simulated; this is presented in Figure 3 and listed in Table 1.

It should be noted that the κ-values reported for all back-arc (volcanic-arc) stations have very large values (up to 0.8–0.9 in some cases), not usually observed for shallow earthquakes. However, such values are typical for back-arc recordings in subduction areas (e.g., Pozgay et al., 2009) and have been successfully employed to produce a 3D-Q_S tomographic model of the southern Aegean Sea area (Ventouzi et al., 2014). Furthermore, they have been cross-checked with the results from Sea13, who introduced separate terms in their GMPE for the mantle-wedge anelastic attenuation affecting back-arc stations. Though Sea13 determined anelastic attenuation from peak values (time domain) and the κ-value dataset of Ventouzi et al. (2013) is based on spectral estimates, the results from both studies are in very good agreement for the frequency range of interest (1–10 Hz). Specifically, the average κ difference between back-arc and fore-arc stations obtained from the dataset of Ventouzi et al. (2013) leads to ground-motion differences similar to the corresponding bias predicted by the Sea13 relation (see Ⓔ Table S2, available in the electronic supplement to this article) for frequencies between 1 and 10 Hz. This observation suggests that the employed κ-values (and the resulting Q_S model) are compatible with the time-domain characteristics of seismic motions for the intermediate-depth events of the southern Aegean Sea area.

Geometrical Spreading and Frequency-Dependent Q_S Model

The geometrical spreading was taken to be equal to r^{-1}, assuming an effective half-space propagation pattern, following previous work for intermediate-depth events in the area (e.g., Benetatos and Kiratzi, 2004, or the detailed analysis of the Kythera event by Boore et al., 2009). Moreover, the main anelastic attenuation parameters employed for the simulations were based on the conceptual attenuation model presented in Figure 2 and the regression results of Sea13. Initially, we constrained the background anelastic attenuation, which corresponds to waves that are not affected by either the high-attenuation back-arc mantle wedge or the presence of possible in-slab wave channeling (solid rays in Fig. 2). To create an appropriate model for our simulations, we computed a frequency-dependent quality factor Q_S (Fig. 7) from Sea13 using the following equation:

$$Q_s = (\pi f)/(\ln(10)c\beta) \tag{4}$$

(e.g., Atkinson and Mereu, 1992), in which c is the absolute value of the anelastic attenuation coefficient and $\beta = 4.0$ km/s is the average shear wave adopted from the 3D velocity structure of Papazachos and Nolet (1997), as was adapted by Boore et al. (2009).

The anelastic attenuation coefficients reported for elastic pseudoacceleration response spectra (PSA) by Sea13 (c_{32} for in-slab earthquakes and c_{41}, c_{42} for interface earthquakes) were used in equation (4), whereas the ln(10) term is due to the use of $\log_{10}$ measures by Sea13. The corresponding results for in-slab events are shown in Figure 7a. It should be noted that although FAS and PSA anelastic decay rates with distance are similar at intermediate frequencies, significant differences can be observed at high frequencies, especially for larger magnitude events, with PSA decay rates being systematically smaller than the corresponding FAS ones (e.g., Cotton et al., 2008). However, the FAS and PSA back-arc anelastic attenuation results presented by Boore et al. (2009) for the Kythera event (M 6.7), which is the largest event used in this work, exhibit very similar values, with the PSA decay rates being in fact slightly larger (~9%) than the FAS ones for the frequency range examined in the present work (0.25–20 Hz). This is verified by Figure 7a, where we also present the Q_S background anelastic attenuation model estimated by Boore et al. (2009), which is practically identical with the present study results.

For interface earthquakes (depths ~45–60 km), Figure 7b shows the corresponding S-wave anelastic attenuation models (Q_S). For these events, we present two different attenuation models, one for fore-arc and one for back-arc stations, following again the classification proposed by Sea13. As noted earlier, the Sea13 results suggest that energy propagation for these shallower subcrustal events is not affected by the high-attenuation volcanic-arc mantle wedge, but is mostly controlled by the average anelastic attenuation
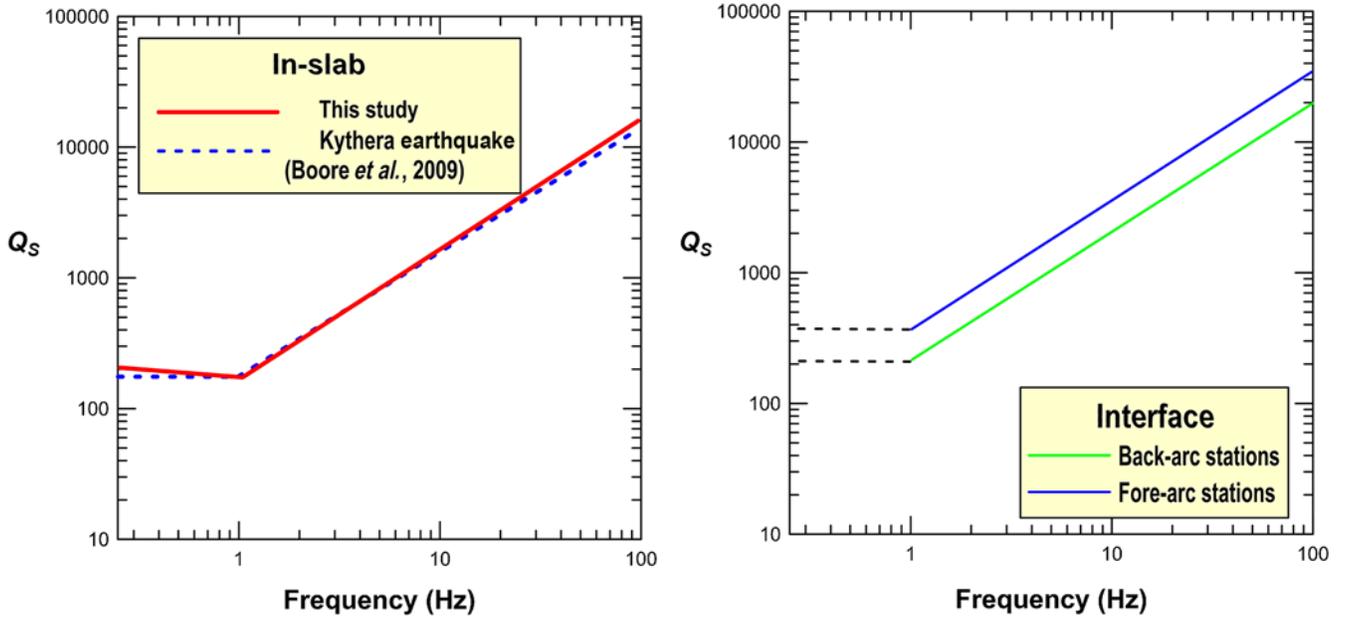
Figure 7. (a) Background Q_S attenuation model for in-slab intermediate-depth earthquakes, estimated on the basis of results from Sea13. The dashed line depicts the Q_S model determined by Boore *et al.* (2009) using data from the Kythera mainshock (8 January 2006, **M** 6.7). (b) Q_S model for interface earthquakes ($h \sim 45$–60 km) adopted through the same procedure. Q_S was assumed to be flat (dashed lines) below 1 Hz, similar to in-slab events, due to the lack of results from Sea13. The color version of this figure is available only in the electronic edition.

properties of the eastern Mediterranean (along-arc) and Aegean Sea (back-arc) upper lithosphere, as also predicted from the model of Figure 2. Sea13 anelastic coefficients for interface events were provided up to 1 Hz. In the absence of reliable information, a flat Q_S variation for the 0.1–1 Hz range was adopted, similar to the pattern observed for in-slab events.

Correction for Back-Arc/Fore-Arc Path Effects

A critical issue for the modeling of in-slab earthquakes concerns the incorporation of the effects of the high-attenuation back-arc area mantle wedge and the outer fore-arc wave channeling along the subducted slab on strong motions, as previously described. For this reason, we incorporated the results obtained by Sea13, who superimposed these effects on the background attenuation model. Specifically, for the modified Sea13 model adopted in this work, the frequency-dependent anelastic attenuation (equation 4) concerns only S waves that cross the Aegean lithosphere (normal waves, depicted by dotted rays in Fig. 2). Waves traveling through the high-attenuation back-arc mantle wedge (dashed rays in Fig. 2) are subject to an additional anelastic attenuation affect. On the other hand, waves channeled through the subducting lithosphere and recorded in the fore-arc (outer-arc) region show a weaker anelastic attenuation with distance than the one predicted by our background anelastic attenuation model

(equation 4), and hence exhibit an apparent amplification/ wave focusing effect, especially at high frequencies.

In the Sea13 model, appropriate coefficients (c_{41} and c_{42}) have been used to control the additional anelastic attenuation of the back-arc region due to the mantle-wedge attenuation, for earthquakes with depths ≥ 100 and < 100 km, respectively. Additional coefficients (c_{51} and c_{52}) have been employed to account for the additional slab amplification of earthquakes with depths ≥ 100 and < 100 km, respectively, for the fore-arc region. According to Sea13 results and the model of Figure 2, the previous attenuation/amplification factors for deeper events ($h \geq 100$ km) do not depend on hypocentral distance, that is, they are fixed for both back-arc and fore-arc cases. For example, waves from deep events ($h > 100$ km) have to cross the same distance within the high-attenuation mantle wedge, hence are subject to roughly the same (fixed) additional anelastic attenuation effect. This is not the case for the shallower events ($h < 100$ km), for which the additional attenuation/amplification can be observed after a certain critical distance when normal waves (as depicted in Fig. 2) start to be influenced by the mantle wedge/subducting slab effects. For these events, an appropriate distance weighting factor, $f(h, R)$, modulates the amplitude of this additional attenuation/amplification (see Sea13 for details). The final back-arc (attenuation) and fore-arc (amplification) factors Y can be estimated for in-slab events by the following equation:

$$Y = \begin{cases} 10^{c_{41}} \, (h > 100 \text{ km}) & 10^{c_{42}f(h,R)} \, (h \leq 100 \text{ km}) \text{ back-arc area (ARC} = 0 \text{ in Sea13)} \\ 10^{c_{51}} \, (h > 100 \text{ km}) & 10^{c_{52}f(h,R)} \, (h \leq 100 \text{ km}) \text{ along-arc area (ARC} = 1 \text{ in Sea13)} \end{cases}, \tag{5}$$

Table 2

Frequency-Q_S Values for In-Slab and Interface Events Presented in Figure 7

Type	f (Hz)	Q_S
In-slab	0.25	218
	1.0	191
	100	16,554
Interface/back-arc	0.25	(210)
	1.0	210
	100	19,821
Interface/fore-arc	0.25	(362)
	1.0	362
	100	34,436

Values in parentheses correspond to extrapolated values, following the pattern of in-slab events.

Table 3

Amplification/Attenuation Factors

f (Hz)	MYKO	ZKR
0.2	0.66	1.3
0.5	0.73	1.57
1	0.63	2.07
2.5	0.37	2.88
5	0.25	2.49
10	0.31	2.83
20	0.33	2.57
40	0.32	2.6
100	0.33	2.66

Spectral attenuation/amplification values for the 7 October 2004, **M** 5.5, $h \sim 130$ km earthquake for two stations (MYKO and ZKR) depicted in Figure 4.

in which h is the focal depth and c_{41}, c_{42}, c_{51}, c_{52}, and $f(h, R)$ are appropriate frequency-dependent coefficients (see table 2 of Sea13, also provided as Ⓔ Table S2).

Following the previous scheme, additional spectral attenuation/amplification values were computed for all back-arc/fore-arc stations for in-slab events using equation (5). As an example, we present in Table 3 the corresponding spectral attenuation/amplification values estimated for stations ZKR (along-arc) and MYKO (back-arc), for the 7 October 2004 in-slab event (**M** 5.5, $h \sim 130$ km, event 6 in Table 1), located at roughly the same hypocentral distance (∼200 km). It is evident that the proposed spectral difference at high frequencies, as predicted by the Sea13 model, is almost 1 order of magnitude and is expected to significantly affect the strong-motion modeling, especially PGA and high-frequency FAS values. It should be noticed that both these factors do not depend on distance; hence they cannot be directly included in equation (4), as we did, for example, for the anelastic attenuation factors of interface earthquakes (Table 2). Therefore, it was necessary to introduce them as fixed (distance-independent) spectral modulation effects. Implementation of factors that control the source spectral content in EXSIM_DMB is typically performed through two separate files that control crustal and site amplification effects. In our case, we introduced these additional anelastic attenuation/slab amplification effects by including frequency-dependent attenuation/amplification values (like those of Table 3) through the EXSIM_DMB crustal amplification file. For this reason, we generated a combined site/crustal amplification effect, through the corresponding EXSIM_DMB site amplification file. It does not matter how the effects are apportioned between these files, as the individual file contents are multiplied frequency-by-frequency to obtain the effective combined filter used in the simulations.

Because the scheme to determine these files depends on both event and station properties (coordinates, event depth, etc.), custom amplification and parameter files need to be generated for each event-recording station pair and independent EXSIM_DMB runs were performed for each case. The corresponding sample EXSIM_DMB parameter and site

amplification files for stations MYKO and ZKR of event 6 of Table 1 are given in Ⓔ Table S1, whereas the additional spectral attenuation/amplification values introduced to account for back-arc/fore-arc attenuation/amplification effects (included in the EXSIM_DMB crustal amplification file) are the ones already presented in Table 3.

Estimation of Source and Site-Effect Factors

Although events employed in this work span the range **M** 4.5–6.7, the majority of the earthquakes modeled vary between **M** 4.5 and 6.1 (Table 1). Although, a point-source model could be used for the lower magnitude events, we decided to use finite-source models for the whole magnitude range. This approach allowed us to investigate the associated source parameters (e.g., stress parameter) for such simulations and at the same time facilitate the future simulation of larger magnitude events (e.g., historical intermediate-depth earthquakes) in the study area.

In general, fault dimensions for intermediate-depth events are poorly constrained, the main reasons being the absence of aftershock sequences that could delineate the activated area. In the present work, fault dimensions (length and width) were constrained by intermediate-depth slip-model results from waveform inversions published for the Aegean Sea area by Yolsal-Çevikbilen and Taymaz (2012), which are presented in Figure 8. The reported lengths and widths for these intermediate-depth (mostly in-slab) events are almost identical, suggesting that the corresponding rupture areas could be considered as almost square sources. For this reason and considering the uncertainties of the inverted slip models, we employed a single relation (equation 6) to estimate both the length and width for the events listed in Table 1 from their moment magnitude (**M**):

$$\log(D) = 0.45 \times \mathbf{M} - 1.65, \qquad (6)$$

in which D is either fault length or width (in km). This approach is essentially equivalent to providing a calibration of the total rupture area with the moment magnitude because D
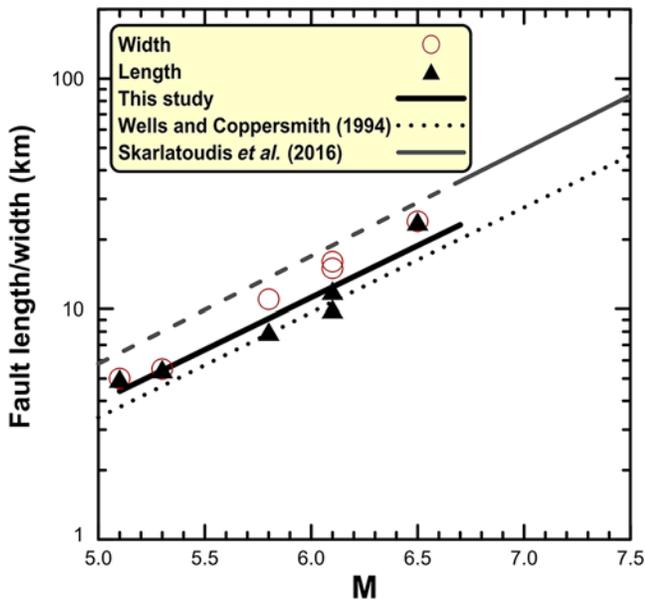
Figure 8. Proposed scaling relation (black thick line) between moment magnitude and fault dimensions (equal length and width) for intermediate-depth events of the South Aegean Sea area, using the fault-slip data of Yolsal-Çevikbilen and Taymaz (2012). The thin gray line corresponds to the square root of the rupture area (equivalent equal length-width size) scaling relation with moment magnitude, for worldwide subduction region earthquakes from Skarlatoudis *et al.* (2016) (the dashed segment depicts the extrapolation outside the magnitude range of the original relation). The corresponding relation for shallow events from Wells and Coppersmith (1994) for all fault types is also depicted for comparison (dotted line). The color version of this figure is available only in the electronic edition.

(equal fault length and width) corresponds to the square root of the rupture area.

For comparison, we also plot in Figure 8 the square root of the rupture area (which corresponds to a fault with equal length and width) for shallow-crustal events (for all faulting types) from Wells and Coppersmith (1994), as well as the corresponding relations proposed by Skarlatoudis *et al.* (2016) for worldwide subduction (interface) event data. Because the latter two relations have been proposed for larger magnitude events (**M** 6.7–9.2), we also present their extrapolation for our magnitude range (**M** 5.1–6.6). It is clear that the employed equation (6) provides estimates between those determined for shallow events and the larger length/width values that are expected from worldwide subduction/interface events, though the corresponding magnitude dependence is rather similar for all relations.

The rupture to shear-wave velocity ratio was set to 0.8, similar to the value used by various researchers for such events (e.g., Benetatos and Kiratzi, 2006; Yolsal-Çevikbilen and Taymaz, 2012). Source shear-wave velocities in the ~4.25–4.6 km/s range were obtained from the 3D-tomographic model of Papazachos and Nolet (1997), whereas densities were estimated from the same model using standard density–V_P relations (Brocher, 2005; see also Boore, 2016). In all cases, we adopted a uniform distributed slip, with a

random starting point, because no information on the fault-slip distribution was available for almost all events. This choice is also imposed because we wanted to have a rather standard source model to use for the simulation of future events, for which the corresponding slip distribution will be unknown. Finally, the dimensions of the subfaults were constrained using the approach of Beresnev and Atkinson (1999), whereas the pulsing percent (number of pulsing subfaults) was set to 50%, following the suggestion of Boore (2009). Site conditions according to Building Seismic Safety Council (BSSC) (1994) and Uniform Building Code (UBC) (1997) for all strong-motion stations were adopted from Sea13a, whereas no site amplifications were considered for velocity broadband stations that were installed on bedrock sites, similar to Boore *et al.* (2009) and Sea13. B, C, and D soil classes according to NERHP/UBC practically coincide with the A, B, and C soil classification used in Eurocode 8 (2004), hence adopting the presented results to the standards locally used is relatively trivial. As site-specific amplifications were not available, generic site amplification functions for each soil class were adopted from the work of Klimis *et al.* (1999, 2006) for the area of Greece, after adjusting them for the difference in density and shear-wave velocity of the local 1D velocity model (Boore *et al.*, 2009). An alternative that can also be employed for future simulations would be to employ National Earthquake Hazards Reduction Program soil class on the basis of proxies derived from local geology and/or slope information, for example, as proposed for the area of Greece by Stewart *et al.* (2014). Finally, the adopted value for the stress parameter of the final simulations was estimated from a parametric search approach on the basis of the best fit between the observed and the simulated FAS. For our modeling, we employ a single stress-parameter value for each event (both fore-arc and back-arc stations). Both of these choices (generic site-effect, single-event stress parameter) are motivated by our strategy to formulate a generic standard modeling approach, which can be easily employed for future and past earthquake simulations.

Stress Parameter

We estimated the stress parameter ($\Delta\sigma$) from the stochastic simulation of all earthquakes listed in Table 1. As mentioned earlier, we adopted a trial-and-error approach and tested different stress-drop values, initially through a visual comparison of simulated and observed acceleration Fourier spectra. After determining the preliminary stress-parameter range, we employed steps of 5, 10, and 50 bars for the 10–50, 500–200, and 200–1200 bars ranges, respectively, minimizing the total root mean square (rms) misfit between observed and simulated FAS in the 0.25–20 Hz frequency range for all records available for each event. We did not further fine-tune the final stress-parameter values (e.g., by determining the actual values that correspond to the absolute minimum rms), as the involved uncertainties in the
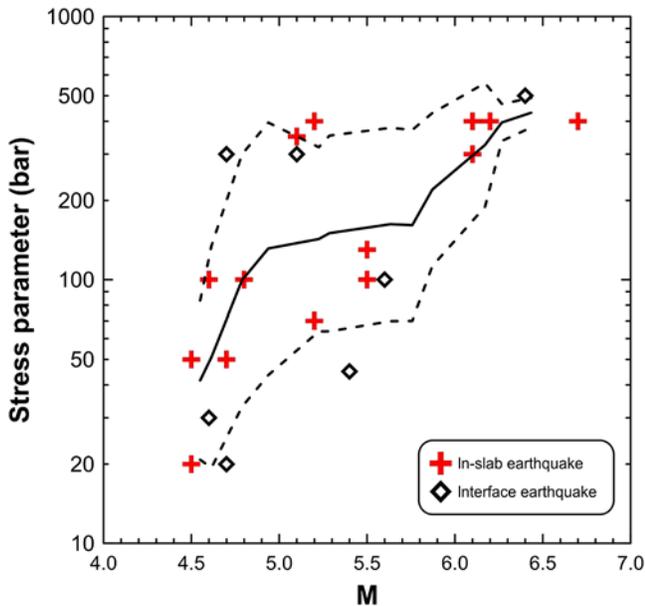
Figure 9.   Stress-parameter values for in-slab and interface earthquakes of the South Aegean Sea area, estimated from stochastic modeling, versus moment magnitude. The solid line corresponds to a seven-point moving average of the data (changed to five- and three-point at the end of the available magnitude range). The ±1 standard deviation values are also depicted with dashed lines. The color version of this figure is available only in the electronic edition.

stress-parameter determination are much larger, as discussed later. The finally determined stress-parameter values for all examined events are presented in Table 1.

Although the $\Delta\sigma$ values determined from stochastic simulations of Aegean Sea area shallow earthquakes lie in the 50–100 bars range (e.g., Margaris and Boore, 1998) similar to worldwide observations, the obtained stress-parameter values for the intermediate-depth earthquakes of the southern Aegean Sea subduction zone reach up to ∼500 bars for **M** 6.7. These high values are in agreement with the high-stress-parameter range (400–600 bars) obtained independently by Boore et al. (2009) for the Kythera 2006 mainshock (8 January 2006, **M** 6.7). Margaris and Hatzidimitriou (2002) also obtained large Brune stress-parameter values (200–300 bars) from strong-motion simulations of two Aegean interface (thrust) events (18 November 1997 **M** 6.6 and 13 October 1997 **M** 6.4), whereas their corresponding stress-parameter values for normal and strike-slip events in the Aegean sea area ranged between 30 and 80 bars. Large Brune stress-parameter values have been also observed from similar simulations for interface events, for example, Macias et al. (2008) reported values of 120–200 bars for the Tokachi-Oki sequence (**M** 5.5–8.1, $h \sim 25$–50 km).

In Figure 9, the estimated $\Delta\sigma$ values are plotted against moment magnitude for both in-slab (crosses) and interface events (diamonds). We also present in the same figure, a seven-point window moving average with a black solid line, as well as its 1 standard deviation relative error (dashed lines). The results do not show systematic differences between the in-

slab and interface earthquakes. Moreover, a positive correlation is found between the derived stochastic stress-parameter values and the moment magnitudes of the examined earthquakes, suggesting that **M** ≥ 6.0 events require quite large stress-parameter values (300–600 bars) for their strong-motion modeling. A similar increase of the Brune stress-parameter values with magnitude has been observed for the Vrancea (Romania) intermediate-depth events by Sokolov et al. (2005), using strong-motion point-source simulations. The same researchers propose stress-parameter values between 300 and 1000 bars for events in the range **M** 6.0–7.1, in good agreement with the results presented in Figure 9. Although stress-parameter values determined for subcrustal events from strong-motion simulations are generally quite large, the magnitude dependence we found may not be a typical feature of intermediate-depth earthquakes. For example, although Wong et al. (2015) also obtained high stress-drop parameters (∼70–400 bars, median: 113 bars) for subcrustal ($h \sim 20$–50 km) Hawaiian events from point-source simulations, no magnitude dependence of the stress-parameter values was observed in their study.

Strong Ground Motion Modeling

We used the EXSIM_DMB code with the previously described source, path, and site parameters to calculate synthetic waveform records and their FAS. Figure 10 presents a PGA and PGV comparison of recorded (combining the two horizontal components using the RotD50 measure, as introduced by Boore, 2010) and synthetic values for all stations, as well as between horizontal-component FAS for two back-arc stations (APE and MYKO) and two stations located along the Hellenic fore-arc area (ZKR and ARG) for event 6 of Table 1 (**M** 5.5, $h = 130$ km). The PGA/PGV comparisons clearly identify the large fore-arc to back-arc differences for both real and synthetic data, as well as the larger effect (∼1 order of magnitude) on the PGA values, which are richer in higher frequency spectral content thus more prone to anelastic attenuation effects. For the FAS comparison, although all four stations are located almost at the same hypocentral distance, the two stations along the Hellenic outer-arc exhibit roughly 1 order of magnitude higher peak FAS values than the back-arc ones. For all studied sites, the synthetic FAS (thick black lines) exhibits a similar pattern with the observed ones for the frequency range of interest (0.25–20 Hz), nicely capturing the very large differences between fore-arc and back-arc area. The observed agreement for both peak and spectral values suggests that although a large number of modeling parameters are involved in the stochastic simulations (reported in Table 4 for this event), the adopted frequency-dependent anelastic attenuation and slab amplification model allowed us to efficiently simulate such complicated propagation effects observed in the recordings.

For the FAS simulations of Figure 10, we also present the predicted spectra for stress parameters that differ by a factor of 2 with respect to the determined value for this
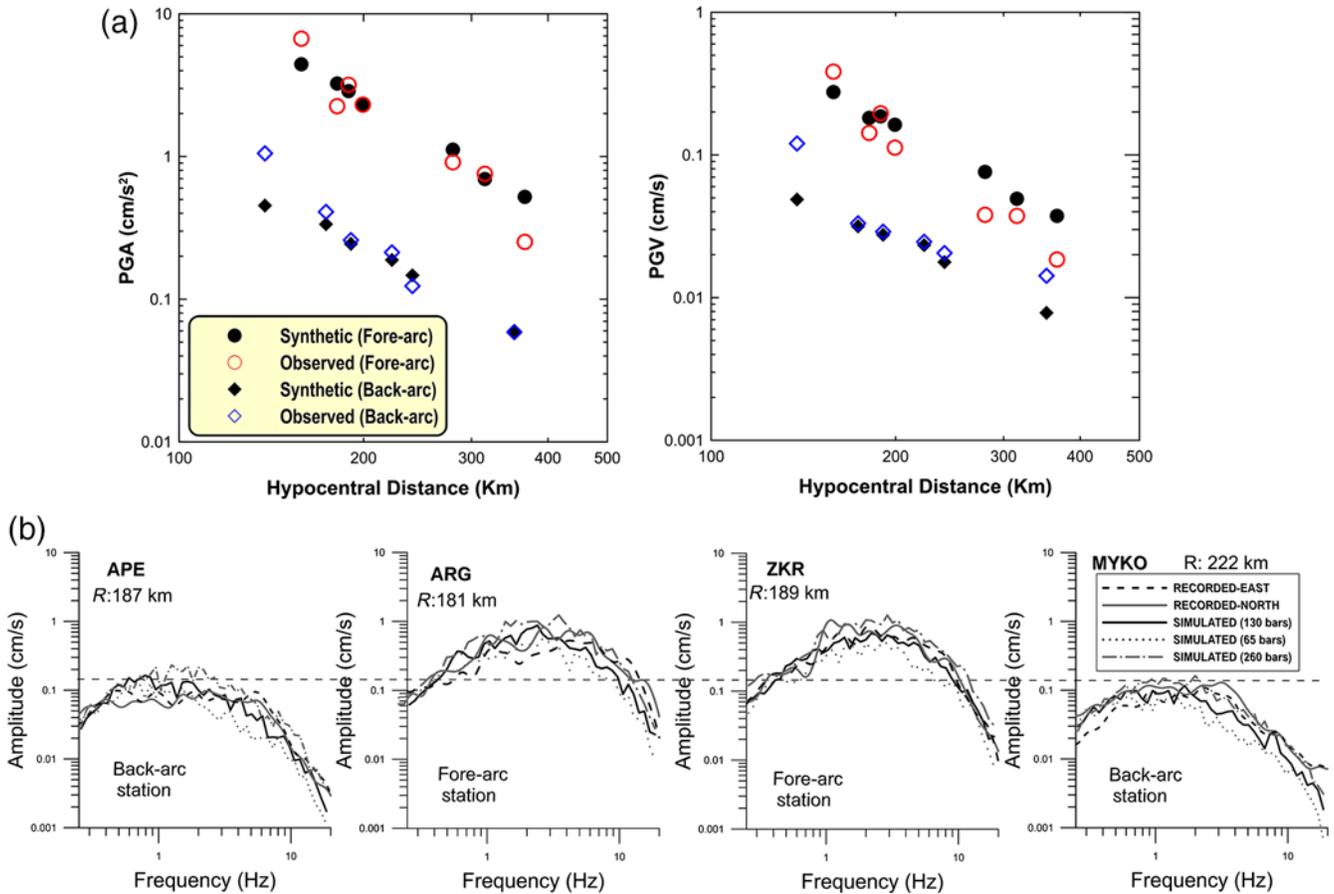
Figure 10. (a) Comparison of the observed (RotD50) peak ground acceleration (PGA) and peak ground velocity (PGV) values, against stochastic simulation synthetics for the 7 October 2004 in-slab event (**M** 5.5, $h = 130$ km, event 6 in Table 1; see Fig. 4). Notice the large back-arc to fore-arc differences in both datasets. (b) Observed and predicted Fourier amplitude spectra (FAS) for back-arc (APE and MYKO) and fore-arc (ZKR and ARG) stations for the same event (0.25–20 Hz). Although all stations lie roughly at the same hypocentral distance, fore-arc stations exhibit almost 1 order of magnitude higher FAS values than back-arc stations. The color version of this figure is available only in the electronic edition.

earthquake. From the individual fits, as well as the intersta-tion variability of the FAS fits, it is clear that this is an appropriate error factor to be considered for the stress param-eter of these events. This suggestion is also confirmed by the blind prediction test later presented. Moreover, the relative standard error of the stress-parameter moving average in Figure 9 corresponds to value of ~2.1, suggesting that an average 2× error factor should be employed for the stress-parameter value in similar simulations.

The FAS plots presented in Figure 10 suggest that the strong back-arc anelastic attenuation also has a secondary effect, not only reducing but also shifting the peak FAS am-plitudes to much lower frequencies. For example, although fore-arc station ZKR exhibits a peak FAS value at frequencies ~4–5 Hz, back-arc station APE shows a much lower peak FAS value, roughly at ~1.0 Hz. This FAS amplitude/frequency effect is clearly recognized in Figure 11a and 11b, where we present the distance variation of observed and simulated peak FAS amplitudes and the comparison of observed and simulation peak FAS frequencies, respectively.

As can be clearly seen in Figure 11a, the back-arc and along-arc peak FAS differ by ~5–10 times, a feature captured by the overall trend of the synthetic results. This amplitude bias is also associated with a peak frequency shift, as seen in Figure 11b. Although the synthetic data fail to match the detailed variation of peak FAS frequencies, they clearly predict large differences between back-arc and fore-arc, similar to those shown by the data, with a shift occurring at ~2 Hz when we move from fore-arc (> 2 Hz) to back-arc (< 2 Hz) stations.

Figure 11c,d presents the corresponding spatial distribu-tion of the peak FAS frequencies for the observed and syn-thetic data. Though small-scale variations are found between the real and synthetic data observations, mainly due to local resonant frequencies that are not captured by the generic transfer functions employed in this work, it is clear that the dominant frequency content is mainly controlled by the back-arc or fore-arc character of each recording station. Sim-ilar results can be observed in Figure 11e,f, where the cor-responding spatial distribution of peak FAS amplitudes is presented, revealing a very anomalous spatial pattern of
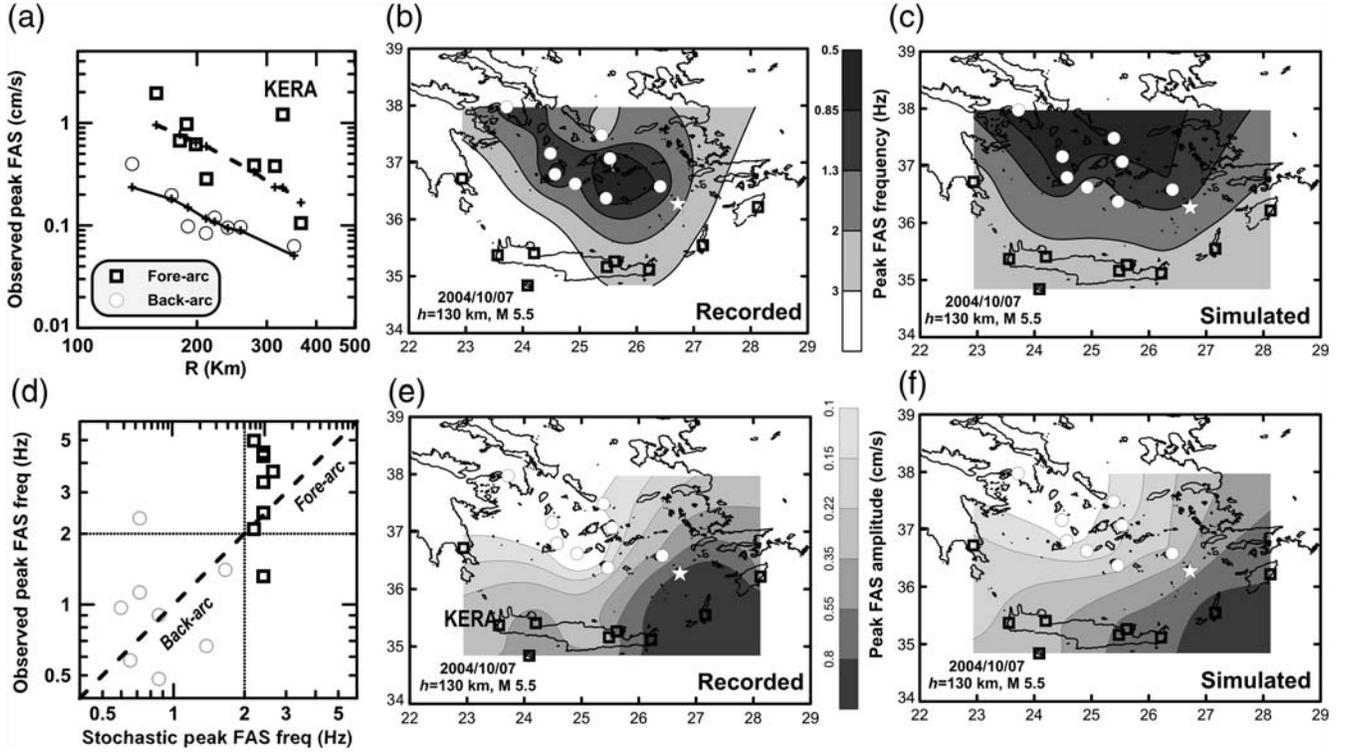
Figure 11. (a) Variation of peak FAS amplitude against hypocentral distance for back-arc (circles) and fore-arc stations (squares) for event 6 of Table 1. The corresponding simulated values are depicted with crosses (back-arc, solid line; fore-arc, dashed line). (b,c) Spatial distribution of the peak FAS frequency of the observed (upper figure) and simulated (lower figure) waveforms. (d) Comparison of peak FAS frequencies for the same event for observed and simulated data. The bisection, as well as the fore-arc to back-arc transition frequency at ~2 Hz are also depicted with dashed and dotted lines, respectively. (e,f) Same for the peak FAS amplitudes. An extremely inhomogeneous spatial pattern is recognized, with respect to the epicenter (denoted by a star).

seismic motions, with respect to the epicenter. Specifically, the largest peak FAS amplitudes are recognized for the southeastern Hellenic arc (Karpathos island, eastern Crete), at a significant distance from the epicenter, whereas seismic motions almost disappear at a similar distance toward the back-arc area, similar to the pattern of peak ground motions (e.g., Figs. 4 and 11). As earlier noted, this specific spatial pattern is in excellent agreement with historical observations of macroseismic damage from large in-slab events (Papazachos and Comninakis, 1969, 1971; Papadopoulos *et al.*, 2002). Furthermore, the good reconstruction of the observed spatial distribution of peak FAS frequencies and amplitudes by the synthetic data verifies the successful ground-motion reconstruction using the modeling discussed in this article. For Figure 11e,f, we have excluded the observations at station KERA, which exhibits anomalously high FAS amplitude values (see also Fig. 11a). The review of the station spectra and horizontal-to-vertical ratios verifies the presence of very strong local amplification phenomena. This observation suggests that although generic site effects may be appropriate to capture the main contribution of local site effects on the examined events, detailed knowledge of site effects is necessary to improve the model efficiency.

Despite the previously presented complex spatial patterns of ground motions (e.g., largest observations not

located at the epicenter), the good agreement between observations and synthetics is verified by Figure 12a,b, where the comparison between PGA and PGV values is presented for the entire dataset (Table 1) including more than 600 records. In general, a good agreement between peak ground-motion measures and predictions is observed for the entire data range, with reasonable variance and almost no bias. In general, PGV values show a slightly smaller rms misfit, clearly suggesting that the model is more reliable for intermediate frequencies that are not affected as high frequencies from the complicated anelastic attenuation affects.

To confirm the previous results for the entire frequency range examined in the present work (0.25–20 Hz), we also calculated the overall FAS spectral misfit for all records. The average FAS spectral ratio bias between observed and simulated data $B(f)$ was estimated using the following equation:

$$r_j(f) = \ln\left[\frac{A_j^{\text{Observed}}(f)}{A_j^{\text{Simulated}}(f)}\right] \tag{7}$$

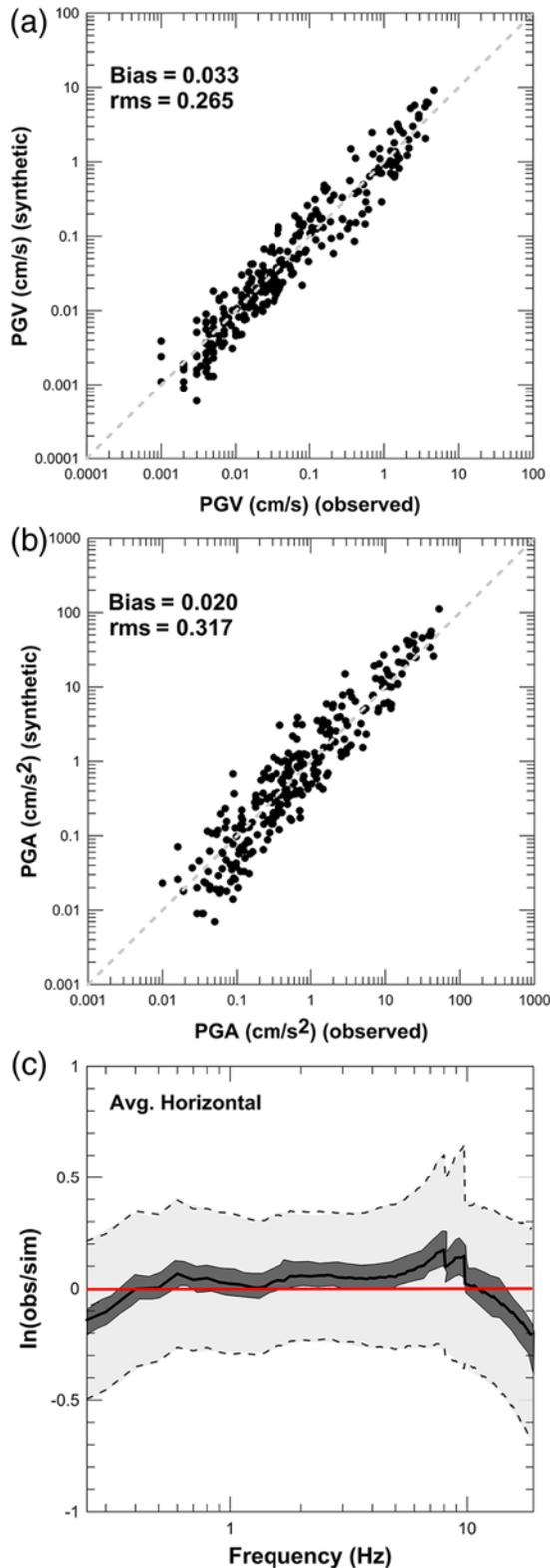$$B(f) = \frac{1}{N}\sum_{j=1}^{N} r_j(f) \tag{8}$$

Figure 12. Comparisons of observed and simulated (a) PGV and (b) PGA. (c) Model bias (black line) and standard error (light shaded region) for FAS in the frequency range examined (0.25–20 Hz). The dark shading shows ±90% confidence limits on the mean bias. The simulated PGA, PGV, and FAS bias/root mean square (rms) values were estimated for all events listed in Table 1. The color version of this figure is available only in the electronic edition.

(e.g., Graves and Pitarka, 2010), in which $A_j(f)$ denotes the spectral amplitude of observation j at frequency f and N corresponds to the total number of observations. The standard error of the average spectral ration is given by

$$\sigma(f) = \left\{ \frac{1}{N} \sum_{j=1,N} [r_j(f) - B(f)]^2 \right\}^{0.5}. \qquad (9)$$

The overall FAS performance of our calibrated model is presented in Figure 12c for the examined frequency range (0.25–20 Hz). In general, the overall FAS bias is small, with small deviations around zero and relatively small standard errors (typically in the ∼0.25–0.4 range). A slightly larger FAS bias is observed for $f > 8$ Hz, locally up to ∼ ± 0.2. Visual inspection of the data FAS suggests that in most cases this is due to the presence of high-frequency amplification effects (especially at some hard soil stations) or the presence of stronger high-frequency attenuation (e.g., due to 3D anelastic attenuation effects), not correctly recovered by the attenuation model employed in the present work. However, Figure 12c suggests that the overall performance of the employed stochastic modeling can be considered as satisfactory, regarding both peak ground motion and FAS values.

Result Validation

To further validate the adopted approach, we used data from a recent intermediate-depth earthquake that has not been used in the original analysis, namely the 24 July 2015 **M** 5.0 Nisyros earthquake (epicenter ∼15 km southwest of Nisyros, $h = 133$ km), and applied the same procedure with the proposed EXSIM parameterization (Table 5). The focal mechanism showed strike-slip faulting with significant thrust component, in excellent agreement with the regional tectonic environment for such events. Because of the relatively small fault dimensions (∼4 × 4 km, equation 6), the choice of the fault plane is not expected to affect the simulation results. The main difference for this blind test, in comparison to the results presented for all events in Table 1, is that the stress parameter was not optimized using a trial-and-error approach but was simply set to a typical value of 130 bars, as suggested from the plot of Figure 9, similar to what would be employed for simulations of possible future events.

In Figure 13, we compare the observed and predicted acceleration PGA and PGV values, as well as the FAS values in the 0.25–20 Hz range from this blind test, where all model parameters (including the stress parameter) are fixed. We also present simulations for stress-parameter values that differ by a factor of 2 from the optimal value determined from Figure 9, considering this factor as a typical stress-parameter uncertainty, in accordance with the previous discussion. In general, the results obtained for this earthquake can be considered as quite satisfactory for almost all stations, located both in the back-arc and fore-arc areas. In all cases, the observed amplitudes of the FAS are well modeled, revealing especially the effect of the high-attenuation back-arc area.

Table 4
Stochastic Model Parameters

Stations	ZKR	MYKO
Shear-wave velocity (V_S)	4.56 km/s	
Density (ρ)	3.22 kg/m^3	
Geometric spreading (R^b)	$b = -1$ (all distances)	
Anelastic attenuation model	As shown in Figure 7a	
Crustal amplification file	Slab amplification factors based on Sea13 (Table 3)	Mantle-wedge attenuation factors based on Sea13 (Table 3)
κ_0	0.084 s (region 9, Fig. 6a)	
Fault-plane orientation	Strike, 75°; dip, 81°; Z_{tor}, 126 km (Fig. 3)	
Fault length and width	Equation 6	
Rupture propagation speed	$0.8 V_S$	
Stress parameter	130 bars (best-fit estimate)	
Site amplification empirical factors	Klimis et al. (1999, 2006), after adjustment for crustal amplification effects following (Boore et al., 2009) (Ⓔ Table S1, available in electronic supplement to this article)	
Slip distribution	Uniform, random starting point	

Input parameters for EXSIM_DMB for two selected stations (ZKR and MYKO) for the 7 October 2004, **M** 5.5, $h \sim 130$ km earthquake (event 6 in Table 1) (see also Ⓔ Table S1).

Table 5
Stochastic Model Parameters

Shear wave velocity (V_S)	4.59 km/s
Density (ρ)	3.24 kg/m^3
Crustal amplification file	Amplification/attenuation factors based on Sea13 (Table 3)
κ_0	0.084 s (region 9, Fig. 6a)
Fault-plane orientation	Strike, 87°; dip, 22°; Z_{tor}, 131 km
Stress parameter	130 bars (Fig. 9)

Input parameters for EXSIM_DMB for the 24 July 2015 Nisyros intermediate-depth earthquake (**M** 5.0, $h \sim 133$ km). Parameters not listed are identical to those reported in Table 4.

For example, stations ARG and YER exhibit almost an order of magnitude difference of their peak FAS values, despite the fact that they are located very close and roughly at the same hypocentral distance (see Fig. 4). It should also be noticed that the method performs well even for the most distant stations (e.g., stations VLI and VLY, located at epicentral distances >300 km), exhibiting a similarly good fit between observed and synthetic FAS. Although FAS values lie mostly within the limits set by the synthetics (stress parameter 65–260 bars), the selected stress-parameter value of 130 bars from Figure 9 exhibits a better fit with most observed FAS distributions. The FAS variability verifies that the relative error factor of 2 observed in the magnitude–stress-parameter scaling of Figure 9 should be considered for all modeling. On the other hand, although a slightly different stress parameter would most probably result in a better fit, the good fit presented in Figure 13 suggests that the stress-parameter values proposed in Figure 9 can be employed for realistic blind predictions of future and past events (e.g., deterministic hazard assessment, modeling of historical events, etc.).

The good reconstruction of the spatial variations of the ground motions is also seen in Figure 14a, where we present the observed and predicted PGA values for the Nisyros blind-test event considered here. The same spatial pattern seen for the peak FAS amplitudes in Figure 11 is observed for the PGA distribution, with the volcanic arc acting as a limit for large PGA values. The largest PGA values are observed in the fore-arc area, at a distance of more than 100 km from the epicenter, similar to Figure 11. It should be noticed that this pattern is essentially controlled by the high levels of back-arc attenuation for events with depths >100 km, as these are expressed through equation (5). The spatial pattern of ground motions significantly changes for shallower depths, as can be seen by the example of Figure 14b, where we present the same PGA distributions for the much shallower ($h = 75$ km) 1 April 2011, **M** 6.1 east Crete event. It is clear that although the observed PGA pattern is still quite different from distributions observed for conventional shallow events, the effect of back-arc attenuation and fore-arc amplification is much more limited. The similarity of observed and modeled data further suggests that the stochastic simulation employed is also efficient for shallower Benioff-zone events in the southern Aegean area. Moreover, larger ground motions may also be observed in the volcanic-arc area from similar in-slab events with depths between 60 and 100 km, not very different from those in the fore-arc area.

Conclusions

Although stochastic simulations of seismic motions have been mainly employed for shallow earthquakes, we presented here an approach that addresses the case of intermediate-depth earthquakes of the Hellenic subduction arc (south Aegean Sea), which exhibit extreme spatial variations mainly due to the high-attenuation back-arc (volcanic-arc) area. For this reason, we employed the EXSIM_DMB code (Motazedian and Atkinson, 2005, as modified by Boore, 2009), and calibrate the corresponding source, path, and site-effect parameters on the basis of previously published results regarding the geophysical structure and the proposed GMPEs for the intermediate-depth earthquakes of the study area. Results are presented not only for both typical peak ground-motion measures (PGA and PGV) but also for FAS, and allow capturing the effect of the attenuation structure not only on the amplitudes but also on the frequency content of the simulated waveforms.

The results obtained in the present study show that the complicated phenomena affecting wave propagation in the southern Aegean Sea subduction area (back-arc mantle wedge attenuation, high-frequency in-slab energy propaga-
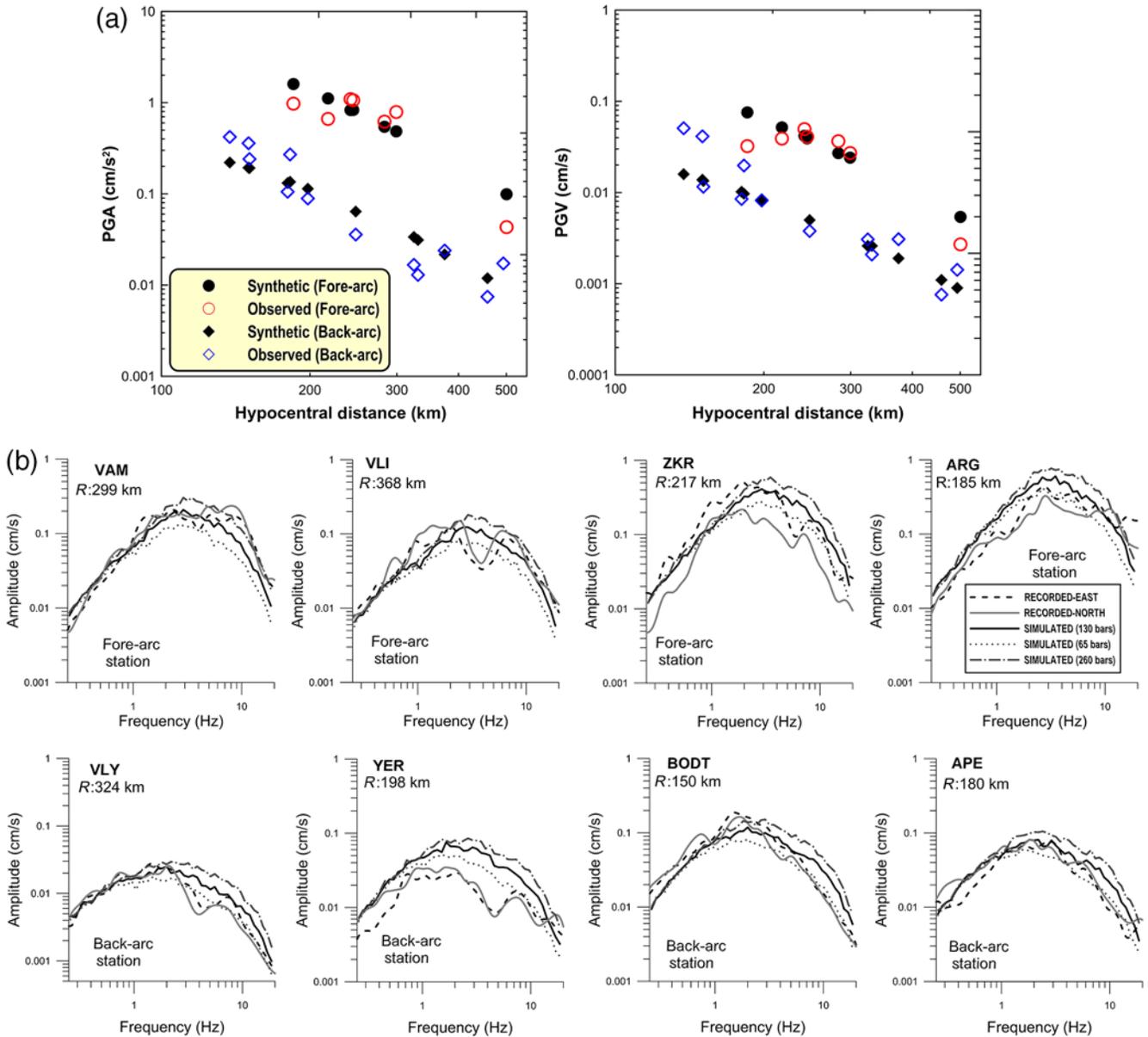
Figure 13. (a) Comparison of the observed (RotD50) PGA and PGV values, against stochastic simulation synthetics for the 24 July 2015 Nisyros intermediate-depth earthquake (**M** 5.0, $h = 133$ km). Notice the large back-arc to fore-arc differences in both datasets. (b) Comparison of the observed (gray and dashed lines) and predicted (thick black line) horizontal-component acceleration FAS (0.25–20 Hz) at eight recording sites for the 24 July 2015 Nisyros intermediate-depth earthquake (**M** 5.0, $h \sim 133$ km) for a typical stress-parameter value of 130 bars, determined from Figure 9, and for stations at different hypocentral distances R. The dotted and dashed-dotted lines are the predicted FAS using a stress-drop parameter relative error of 2, corresponding to 65 and 260 bars, respectively. Notice the good agreement between observed and predicted FAS for almost all sites. The color version of this figure is available only in the electronic edition.

tion, etc.) can be efficiently included in the stochastic simulation approach (EXSIM code) to retrieve the main spectral features of the waveforms of intermediate-depth earthquakes for both along-arc and back-arc stations. This is also confirmed by the additional blind simulation using data not included in the original parametric analysis. These observations suggest that the proposed approach can be employed to simulate ground motions for future, large and moderate intermediate-depth earthquakes in the southern Aegean Sea subduction area. Moreover, an interesting pattern of a signifi-

cant stress-parameter increase for larger events is observed from the results, requiring very large values (300–600 bars) for the modeling of **M** > 6.0 events. This increase is important, regarding not only its possible implication for processes related with the genesis of intermediate-depth events, but also its implications for the study of large, historical intermediate-depth events of the southern Aegean Sea arc.

It is clear that the proposed modeling approach exhibits certain limitations. Finite-fault simulations, while more accurate for large events (**M** 6.0+), are most probably unnecessary
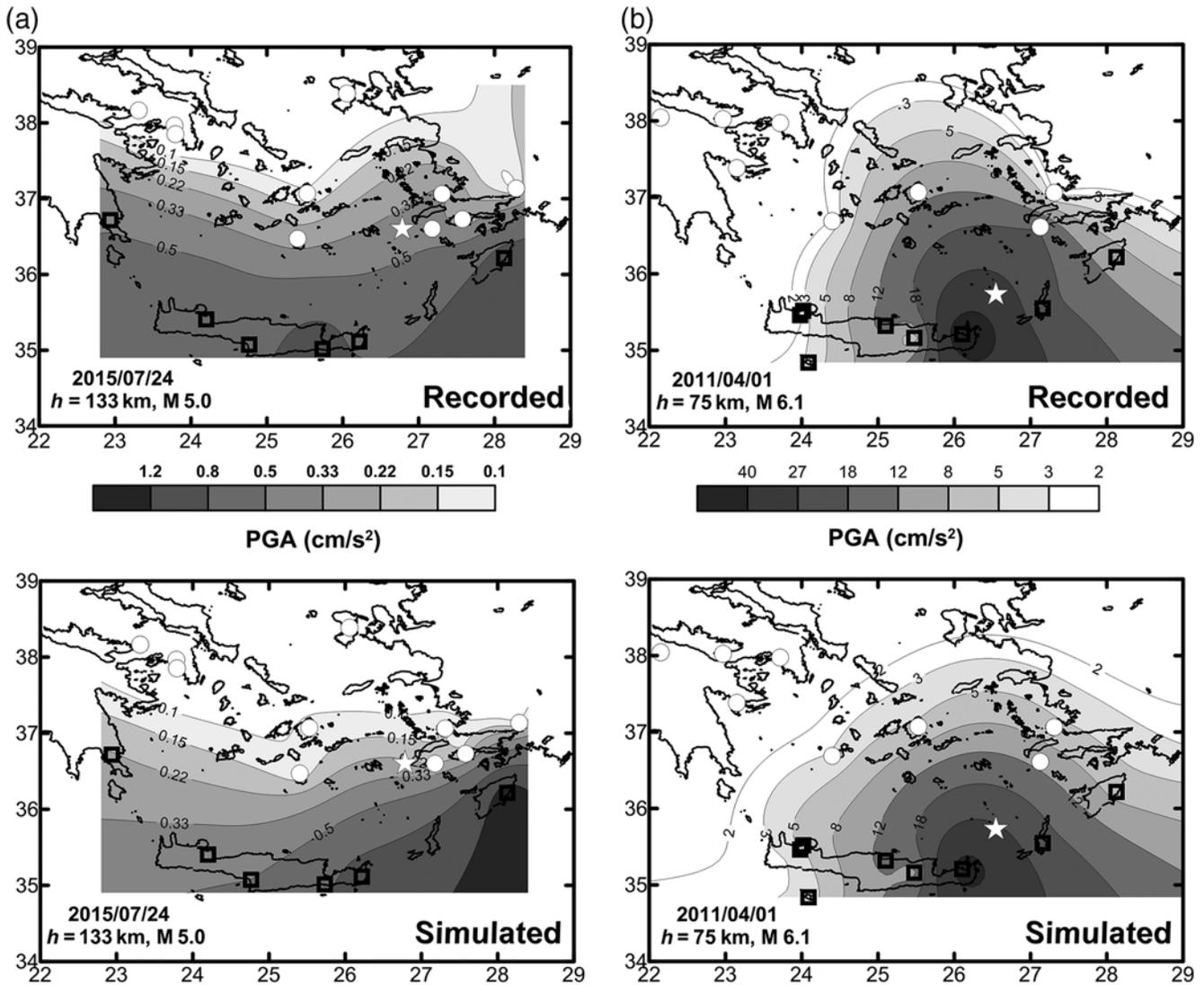
Figure 14.   Observed and simulated spatial variations of PGA values for (a) the deeper ($h = 133$ km) blind test of the 24 July 2015 **M** 5.0 Nisyros earthquake, and (b) the much shallower ($h = 75$ km) 1 April 2011 **M** 6.1 east Crete event. Although the simulated PGA values capture the observed spatial variation patterns, significant differences can be observed between the two events, reflecting the different back-arc attenuation contribution of the mantle wedge as a function of depth. Epicenters are depicted by stars in all maps.

for smaller events that could be possibly modeled by simpler point simulations. In several cases, the depth-dependent back-arc attenuation and fore-arc amplification modeling (employed mainly through equation 5) fails to describe complex but systematic 3D attenuation/amplification phenomena, resulting in poor data fits. Moreover, local site effects that cannot be captured by the generic amplifications employed in this work are clearly present and evident in observed-simulated FAS comparisons for some stations, especially at higher frequencies. The last two factors can be clearly improved with additional future work: site effects can be better introduced in the modeling using site-specific transfer functions. Moreover, a 3D frequency-dependent Q_S model can be developed on the basis of the available κ-value database, allowing single source-path-site κ-value that would also incorporate 3D effects, without the need of additional attenuation operators such as the

ones introduced by equation 5. Finally, simulation tests on larger, historical events, employing damage (macroseismic) data would allow further evaluation of the model reliability and its applicability for seismic hazard assessment for inter-mediate-depth events of the southern Aegean Sea subduction zone.

Data and Resources

Broadband velocity-sensor data used in this study were collected from the EGELADOS (Exploring the Geody-namics of Subducted Lithosphere Using an Amphibian Deployment of Seismographs) and CYCNET temporary net-works, as well as permanent stations archived by GEOFON, all available from the corresponding online archive http:// geofon.gfz-potsdam.de/waveform/archive (last accessed

June 2017). Additional broadband velocity-sensor data were collected from permanent Greek seismological networks, operated by the Hellenic Unified Seismological Network (HUSN), available to the public upon request from individual HUSN members. Acceleration-sensor data employed in this work were collected from the permanent networks operated by the Institute of Engineering Seismology and Earthquake Engineering (ITSAK) and the National Observatory of Athens, which are also available upon request. The focal mechanism of the 2015 Nisyros event was obtained from the Institute of Geodynamics, National Observatory of Athens (http://bbnet.gein.noa.gr, last accessed June 2017). The EXSIM_DMB code used for the simulations is available at http://www.daveboore.com/software_online.html (last accessed June 2017). Several plots were made using the Generic Mapping Tools v.4 (Wessel and Smith, 1998; http://www.soest.hawaii.edu/gmt/, last accessed June 2017).

Acknowledgments

References

Abrahamson, N., N. Gregor, and K. Addo (2015). BC Hydro ground motion prediction equations for subduction earthquakes, *Earthq. Spectra* **32,** 23–44.

Ambraseys, N. N., and R. D. Adams (1998). The Rhodes earthquake of 26 June 1926, *J. Seismol.* **2,** no. 3, 267–292.

Ameri, G., A. Emolo, F. Pacor, and F. Gallovic (2011). Ground-motion simulations for the 1980 M 6.9 Irpinia earthquake (southern Italy) and scenario events, *Bull. Seismol. Soc. Am.* **101,** no. 3, 1136–1151, doi: 10.1785/0120100231.

Anderson, J. G., and S. E. Hough (1984). A model for the shape of the Fourier amplitude spectrum of acceleration at high frequencies, *Bull. Seismol. Soc. Am.* **74,** no. 5, 1969–1993.

Arrigo, G., Z. Roumelioti, C. Benetatos, A. Kiratzi, A. Bottari, G. Neri, D. Termini, A. Gorini, and S. Marcucci (2006). A source study of the 9 September 1998 (M_w 5.6) Castelluccio earthquake in southern Italy using teleseismic and strong motion data, *Nat. Hazards* **37,** no. 3, 245–262, doi: 10.1007/s11069-005-4644-1.

Atkinson, G. M., and D. M. Boore (1997). Stochastic point-source modeling of ground motions in the Cascadia region, *Seismol. Res. Lett.* **68,** 74–85.

Atkinson, G. M., and D. M. Boore (2003). Empirical ground-motion relations for subduction zone earthquakes and their application to Cascadia and other regions, *Bull. Seismol. Soc. Am.* **93,** 1703–1729.

Atkinson, G. M., and R. Mereu (1992). The shape of ground motion attenuation curves in southeastern Canada, *Bull. Seismol. Soc. Am.* **82,** 2014–2031.

Benetatos, C., and A. Kiratzi (2006). Source characteristics of the 8 January 2006 (M_w 6.7) intermediate depth Kythera earthquake, *1st European Conf. on Earthquake Engineering and Seismology (ECEES)*, 3–9.

Benetatos, C. A., and A. A. Kiratzi (2004). Stochastic strong ground motion simulation of intermediate depth earthquakes: The cases of the 30 May

1990 Vrancea (Romania) and of the 22 January 2002 Karpathos island (Greece) earthquakes, *Soil Dynam. Earthq. Eng.* **24,** no. 1, 1–9, doi: 10.1016/j.soildyn.2003.10.003.

Beresnev, I. A., and G. M. Atkinson (1997). Modeling finite-fault radiation from the ω^n spectrum, *Bull. Seismol. Soc. Am.* **87,** 67–84.

Beresnev, I. A., and G. M. Atkinson (1999). Generic finite-fault model for ground motion prediction in eastern North America, *Bull. Seismol. Soc. Am.* **89,** 608–625.

Bohnhoff, M., M. Rische, T. Meier, B. Endrun, D. Becker, H.-P. Harjes, and G. Stavrakakis (2004). CYC-NET: A temporary seismic network on the Cyclades (Aegean Sea, Greece), *Seismol. Res. Lett.* **75,** no. 3, 352–359, doi: 10.1785/gssrl.75.3.352.

Boore, D. M. (1983). Stochastic simulation of high-frequency ground motions based on seismological models of the radiated spectra, *Bull. Seismol. Soc. Am.* **73,** 1865–1894.

Boore, D. M. (2003). Analog-to-digital conversion as a source of drifts in displacements derived from digital recordings of ground acceleration, *Bull. Seismol. Soc. Am.* **93,** 2017–2024.

Boore, D. M. (2005). On pads and filters: Processing strong-motion data, *Bull. Seismol. Soc. Am.* **95,** 745–750.

Boore, D. M. (2009). Comparing stochastic point-source and finite-source ground-motion simulations: SMSIM and EXSIM, *Bull. Seismol. Soc. Am.* **99,** no. 6, 3202–3216, doi: 10.1785/0120090056.

Boore, D. M. (2010). Orientation-independent, non geometric-mean measures of seismic intensity from two horizontal components of motion, *Bull. Seismol. Soc. Am.* **100,** 1830–1835.

Boore, D. M. (2016). Determining generic velocity and density models for crustal amplification calculations, with an update of the Boore and Joyner (1997) generic site amplification for $\bar{V}_S(Z) = 760$ m/s, *Bull. Seismol. Soc. Am.* **106,** 316–320.

Boore, D. M., and G. M. Atkinson (1987). Stochastic prediction of ground motion and spectral response parameters at hard-rock sites in eastern North America, *Bull. Seismol. Soc. Am.* **77,** 440–467.

Boore, D. M., K. W. Campbell, and G. M. Atkinson (2010). Determination of stress parameters for eight well-recorded earthquakes in eastern North America, *Bull. Seismol. Soc. Am.* **100,** no. 4, 1632–1645, doi: 10.1785/0120090328.

Boore, D. M., A. A. Skarlatoudis, B. N. Margaris, C. B. Papazachos, and C. Ventouzi (2009). Along-arc and back-arc attenuation, site response, and source spectrum for the intermediate-depth 8 January 2006 M 6.7 Kythera, Greece, earthquake, *Bull. Seismol. Soc. Am.* **99,** no. 4, 2410–2434, doi: 10.1785/0120080229.

Brocher, T. M. (2005). Empirical relations between elastic wavespeeds and density in the Earth's crust, *Bull. Seismol. Soc. Am.* **95,** no. 6, 2081–2092.

Brüstle, A., W. Friederich, T. Meier, and C. Gross (2014). Focal mechanism and depth of the 1956 Amorgos twin earthquakes from waveform matching of analogue seismograms, *Solid Earth* **5,** no. 2, 1027.

Building Seismic Safety Council (BSSC) (1994). FEMA report 222A: *National Earthquake Hazards Reduction Program Recommended Provisions for Seismic Regulations for New Buildings and Other Structures (FEMA 222A), Part 1: Provisions*, Federal Emergency Management Agency, Washington, D.C., 290 pp.

Castro, R. R., A. Rovelli, M. Cocco, M. Di Bona, and F. Pacor (2001). Stochastic simulation of strong-motion records from the 26 September 1997 (M_w 6), Umbria–Marche (Central Italy) earthquake, *Bull. Seismol. Soc. Am.* **91,** 27–39.

Cotton, F., G. Pousse, F. Bonilla, and F. Scherbaum (2008). On the discrepancy of recent European ground-motion observations and predictions from empirical models: Analysis of KiK-net accelerometric data and point-sources stochastic simulations, *Bull. Seismol. Soc. Am.* **98,** no. 5, 2244–2261.

Eurocode 8 (2004). Design of structures for earthquake resistance, Part 1: General rules, seismic actions and rules for buildings, EN 1998–1, European Committee for Standardization (CEN), Brussels, Belgium.

Friederich, W., and T. Meier (2008). Temporary seismic broadband network acquired data on Hellenic subduction zone, *Eos Trans. AGU* **89,** no. 40, 378, doi: 10.1029/2008EO400002.

Graves, R. W., and A. Pitarka (2010). Broadband ground-motion simulation using a hybrid approach, *Bull. Seismol. Soc. Am.* **100,** no. 5A, 2095–2123.

Kilb, D., G. Biasi, J. Anderson, J. Brune, Z. Peng, and F. L. Vernon (2012). A comparison of spectral parameter kappa from small and moderate earthquakes using southern California ANZA seismic network data, *Bull. Seismol. Soc. Am.* **102,** no. 1, 284–300.

Kkallas, C., K. Papazachos, E. Scordilis, and V. Margaris (2013). Re-examining the stress field of the broader southern Aegean subduction area using an updated focal mechanism database, *Bull. Geol. Soc. Greece* **47,** no. 2, 563–573, available at https://ejournals.epublishing.ekt.gr/index.php/geosociety/article/view/11083/11103 (last accessed December 2017).

Klimis, N., B. Margaris, A. Anastasiadis, P. Koliopoulos, and E. Kirtas (2006). Smoothed Hellenic rock site amplification factors, *5th Hellenic Congress of Geotechnical and Geoenvironmental Engineering*, Vol. 2, Xanthi, Greece, 239–246 (in Greek).

Klimis, N. S., B. N. Margaris, and P. K. Koliopoulos (1999). Site-dependent amplification functions and response spectra in Greece, *J. Earthq. Eng.* **3,** no. 2, 237–270, doi: 10.1080/13632469909350346.

Ktenidou, O. J., F. Cotton, N. A. Abrahamson, and J. G. Anderson (2014). Taxonomy of κ: A review of definitions and estimation approaches targeted to applications, *Seismol. Res. Lett.* **85,** no. 1, 135–146.

Ktenidou, O.-J., S. Drouet, N. Theodulidis, M. Chaljub, S. Arnaouti, and F. Cotton (2012). Estimation of kappa (κ) for a sedimentary basin in Greece (EUROSEISTEST): Correlation to site characterization parameters, *Proc. 15th World Conf. of Earthquake Engineering*, Lisbon, Portugal, 24–28 September, 10 pp.

Macias, M., G. M. Atkinson, and D. Motazedian (2008). Ground-motion attenuation, source, and site effects for the 26 September 2003 M 8.1 Tokachi-Oki earthquake sequence, *Bull. Seismol. Soc. Am.* **98,** no. 4, 1947–1963.

Margaris, B. N., and D. M. Boore (1998). Determination of $\Delta\sigma$ and κ_0 from response spectra of large earthquakes in Greece, *Bull. Seismol. Soc. Am.* **88,** no. 1, 170–182.

Margaris, B. N., and P. M. Hatzidimitriou (2002). Source spectral scaling and stress release estimates using strong-motion records in Greece, *Bull. Seismol. Soc. Am.* **92,** no. 3, 1040–1059.

Motazedian, D. (2006). Region-specific key seismic parameters for earthquakes in northern Iran, *Bull. Seismol. Soc. Am.* **96,** no. 4A, 1383–1395, doi: 10.1785/0120050162.

Motazedian, D., and G. M. Atkinson (2005). Stochastic finite-fault modeling based on a dynamic corner frequency, *Bull. Seismol. Soc. Am.* **95,** no. 3, 995–1010, doi: 10.1785/0120030207.

Papadopoulos, G. A., M. Ziazia, A. Plessa, A. Ganas, V. Karastathis, N. Melis, and G. Stavrakakis (2002). Seismic anisotropy in the east Mediterranean lithosphere: The M_w = 6.3 Karpathos intermediate depth earthquake of 22 January 2002 in the Hellenic arc, paper presented at the *XXVII General Assembly of the European Seismological Society*, Genova, Italy, 1–6 September 2002.

Papazachos, B. C. (1990). Seismicity of the Aegean and surrounding area, *Tectonophysics* **178,** nos. 2/4, 287–308.

Papazachos, B. C., and P. E. Comninakis (1969). Geophysical features of the Greek island arc and eastern Mediterranean ridge, *Comptes Rendus Séances Conf. Reunie Madrid* **16,** no. 16, 74–75.

Papazachos, B. C., and P. E. Comninakis (1971). Geophysical and tectonic features of the Aegean arc, *Geophys. Res.* **76,** 8517–8533.

Papazachos, C., and G. Nolet (1997). P and S deep velocity structure of the Hellenic area obtained by robust nonlinear inversion of travel times, *J. Geophys. Res.* **102,** no. B4, 8349–8367.

Papazachos, C. B., P. M. Hatzidimitriou, D. G. Panagiotopoulos, and G. N. Tsokas (1995). Tomography of the crust and upper mantle in southeast Europe, *J. Geophys. Res.* **12,** 405–412.

Pavel, F., and R. Vacareanu (2015). Kappa and regional attenuation for Vrancea (Romania) earthquakes, *J. Seismol.* **19,** 791–799.

Pozgay, S. H., D. A. Wiens, J. A. Conder, H. Shiobara, and H. Sugioka (2009). Seismic attenuation tomography of the Mariana subduction system: Implications for thermal structure, volatile distribution, and slow spreading dynamics, *Geochem. Geophys. Geosys.* **10,** no. 4, doi: 10.1029/2008GC002313.

Roumelioti, Z., A. Kiratzi, and N. Theodulidis (2004). Stochastic strong ground-motion simulation of the 7 September 1999 Athens (Greece) earthquake, *Bull. Seismol. Soc. Am.* **94,** no. 3, 1036–1052, doi: 10.1785/0120030219.

Roumelioti, Z., A. Kiratzi, N. Theodulidis, and C. Papaioannou (2000). A comparative study of a stochastic and deterministic simulation of strong ground motion applied to the Kozani-Grevena (NW Greece) 1995 sequence, *Ann. Geophys.* **43,** no. 4, doi: 10.4401/ag-3666.

Shaw, B., N. N. Ambraseys, P. C. England, M. A. Floyd, G. J. Gorman, T. F. G. Higham, J. A. Jackson, J. M. Nocquet, C. C. Pain, and M. D. Piggott (2008). Eastern Mediterranean tectonics and tsunami hazard inferred from the AD 365 earthquake, *Nature Geosci.* **1,** no. 4, 268–276.

Skarlatoudis, A. A., and B. N. Margaris (2006). Kythera 2006 earthquake: Data processing of strong motion from various digital sensors, *1st European Conf. on Earthquake Engineering and Seismology*, Geneva, Switzerland, 3–8 September 2006.

Skarlatoudis, A. A., C. B. Papazachos, B. N. Margaris, C. Papaioannou, C. Ventouzi, D. Vamvakaris, A. Bruestle, T. Meier, W. Friederich, G. Stavrakakis, *et al.* (2009). Combination of acceleration-sensor and broadband velocity-sensor recordings for attenuation studies: The case of the 8 January 2006 Kythera intermediate-depth earthquake, *Bull. Seismol. Soc. Am.* **99,** no. 2A, 694–704.

Skarlatoudis, A. A., C. B. Papazachos, B. N. Margaris, C. Ventouzi, and I. Kalogeras (2013). Ground-motion prediction equations of intermediate-depth earthquakes in the Hellenic arc, southern Aegean subduction area, *Bull. Seismol. Soc. Am.* **103,** no. 3, 1952–1968, doi: 10.1785/0120120265.

Skarlatoudis, A. A., P. G. Somerville, and H. K. Thio (2016). Source-scaling relations of interface subduction earthquakes for strong ground motion and tsunami simulation, *Bull. Seismol. Soc. Am.* **106,** no. 4, 1652–1662, doi: 10.1785/0120150320.

Sokolov, V., K. P. Bonjer, M. Oncescu, and M. Rizescu (2005). Hard rock spectral models for intermediate-depth Vrancea, Romania, earthquakes, *Bull. Seismol. Soc. Am.* **95,** no. 5, 1749–1765.

Spakman, W., S. Van der Lee, and R. D. Van der Hilst (1993). Travel-time tomography of the European–Mediterranean mantle down to 1400 km, *Phys. Earth Plant. In.* **79,** 3–74.

Stewart, J. P., N. Klimis, A. Savvaidis, N. Theodoulidis, E. Zargli, G. Athanasopoulos, P. Pelekis, G. Mylonakis, and B. Margaris (2014). Compilation of a local V_S profile database and its application for inference of V_{S30} from geologic-and terrain-based proxies, *Bull. Seismol. Soc. Am.* **104,** no. 6, 2827–2841.

Stiros, S. C. (2010). The 8.5+ magnitude, AD 365 earthquake in Crete: Coastal uplift, topography changes, archaeological and historical signature, *Quaternary Int.* **216,** no. 1, 54–63.

Ugurhan, B., and A. Askan (2010). Stochastic strong ground motion simulation of the 12 November 1999 Duzce (Turkey) earthquake using a dynamic corner frequency approach, *Bull. Seismol. Soc. Am.* **100,** no. 4, 1498–1512, doi: 10.1785/0120090358.

Uniform Building Code (UBC) (1997). *Intern. Conf. of Building Officials, USA*, Vol. II, 489 pp.

Ventouzi, C., C. B. Papazachos, C. Papaioannou, P. Hatzidimitriou, and the EGELADOS Working Group (2013). Obtaining information on the Q-structure of the southern Aegean subduction area by spectral slopes from temporary and permanent networks, *Bull. Geol. Soc. Greece* **47,** no. 3, 1366–1375, available at https://ejournals.epublishing.ekt.gr/index.php/geosociety/article/view/10932/10974 (last accessed December 2017).

Ventouzi, C., C. B. Papazachos, C. Papaioannou, P. Hatzidimitriou, and the EGELADOS working group (2014). Q_P and Q_S attenuation

models of the southern Aegean subduction area, *15th European Conf. on Earthquake Engineering & 34th General Assembly of the European Seismological Commission*, Istanbul, Turkey, 25–29 August 2014.

Wells, D. L., and K. J. Coppersmith (1994). New empirical relationships among magnitude, rupture length, rupture width, rupture area, and surface displacement, *Bull. Seismol. Soc. Am.* **84,** no. 4, 974–1002.

Wessel, P., and W. H. F. Smith (1998). New, improved version of the generic mapping tools released, *Eos Trans. AGU* **79,** 579.

Wong, I. G., W. J. Silva, R. Darragh, N. Gregor, and M. Dober (2015). A ground motion prediction model for deep earthquakes beneath the island of Hawaii, *Earthq. Spectra* **31,** no. 3, 1763–1788.

Yazdani, A., and M. Kowsari (2013). Earthquake ground-motion prediction equations for northern Iran, *Nat. Hazards* **69,** no. 3, 1877–1894, doi: 10.1007/s11069-013-0778-8.

Yolsal-Çevikbilen, S., and T. Taymaz (2012). Earthquake source parameters along the Hellenic subduction zone and numerical simulations of historical tsunamis in the Eastern Mediterranean, *Tectonophysics* **536/537,** 61–100, doi: 10.1016/j.tecto.2012.02.019.

Zhao, J. X., J. Zhang, A. Asano, Y. Ohno, T. Oouchi, T. Takahashi, H. Ogawa, K. Irikura, H. K. Thio, P. Somerville, *et al.* (2006). Attenuation relations of strong motion in Japan using site classification based on predominant period, *Bull. Seismol. Soc. Am.* **96,** 898–913.

Geophysical Laboratory
Aristotle University of Thessaloniki
P.O. Box 352-1
GR-54124 Thessaloniki, Greece
chkkalla@geo.auth.gr
kpapaza@geo.auth.gr
xrusven@geo.auth.gr
askarlat@geo.auth.gr
(C.K., C.B.P., C.V., A.S.)

Institute of Engineering Seismology and Earthquake Engineering
(EPPO-ITSAK)
P.O. Box 53
Finikas
GR-55102 Thessaloniki, Greece
margaris@itsak.gr
(B.N.M.)

U.S. Geological Survey
MS 977
345 Middlefield Road
Menlo Park, California 94025
boore@usgs.gov
(D.B.)